International Journal of Plasticity 159 (2022) 103478

Contents lists available at ScienceDirect

International Journal of Plasticity

journal homepage: www.elsevier.com/locate/ijplas

Mechanical, microstructural and *in-situ* neutron diffraction investigations of equi-biaxial Bauschinger effects in an interstitial-free DC06 steel

Markus Härtel [a,*,1], Christian Illgen [a], Tobias Panzner [b], Enrico Bruder [b], Stefan Schmaltz [b,2], Steven Van Petegem [e], Kai Willner [d], Karsten Durst [c], Helena van Swygenhoven [e], Martin F.-X. Wagner [a]

[a] *Chair of Materials Science, Technische Universität Chemnitz, Institute for Materials Science and Engineering, Chemnitz D-09125, Germany*
[b] *Laboratory for Neutron Scattering, NUM, Paul Scherrer Institute, PSI, Villigen CH-5232, Switzerland*
[c] *Material Science Department, Division of Physical Metallurgy, Darmstadt University of Technology, Darmstadt D-64287, Germany*
[d] *Applied Mechanics, Friedrich-Alexander-Universität Erlangen-Nürnberg, Erlangen D-91058, Germany*
[e] *Swiss Light Source, Paul Scherrer Institut, PSI, Villigen CH-5232, Switzerland*

A B S T R A C T

Bauschinger effects typically describe a reduction of yield strength after a load path change under uniaxial loading conditions. Here, we use in-plane loading to investigate, for the first time, Bauschinger effects in the sheet metal DC06 under well-defined equi-biaxial loading conditions: We first performed equi-biaxial tensile tests with cruciform specimens up to different maximum tensile strains. Then, smaller specimens were prepared from the equi-biaxially deformed inner part of the cruciform specimens and subjected to equi-biaxial compression. The mechanical results show that the material exhibits distinct Bauschinger effects when subjected to equi-biaxial load path changes, which differ from similar observations under uniaxial loading. Specifically, biaxial Bauschinger effect factors quickly reach a level of saturation, whereas the uniaxial Bauschinger effect factors keep decreasing. These Bauschinger effects can be rationalized by considering the results of TEM and EBSD investigations at the different stages of biaxial loading, particularly by considering the evolution of dislocation densities and the formation of substructures, which are related to intergranular and intragranular stresses. Furthermore, residual stress measurements by XRD and in-situ neutron diffraction show an increase of compressive residual stresses after equi-biaxial tensile deformation and unloading. These residual stresses facilitate yielding during subsequent equi-biaxial compression and therefore also clearly contribute to the observed Bauschinger effects.

1. Introduction

Many metallic materials exhibit an asymmetric yield behavior after load path changes, for instance, when tension is followed by compression. The associated Bauschinger effect is typically characterized by a decrease in yield strength after the change in load path (Bauschinger, 1886). Many research studies from the last decades (Bate and Wilson, 1986; Buckley and Entwistle, 1956; Caceres et al., 1996; Margolin et al., 1978; Masing, 1926; Mughrabi, 1983; Sleeswyk and Kemerink, 1985; Tan et al., 1994) as well as recent publications (Bagherpour et al., 2020; Demir and Raabe, 2010; Hou et al., 2022; Hu et al., 2017; Kostryzhev et al., 2010; S. W. Lee et al., 2013; Lewandowska, 2003; Marcadet and Mohr, 2015; Richards et al., 2011; Tsuru et al., 2016; Vincze et al., 2005) deal with various

* Corresponding author.
E-mail address: markus.haertel@mb.tu-chemnitz.de (M. Härtel).
[1] Now at thyssenkrupp Dynamic Components Chemnitz GmbH, D-09120 Chemnitz.
[2] Now at Schaeffler Technologies AG & Co. KG, Advanced Simulation, D-91074 Herzogenaurach.

https://doi.org/10.1016/j.ijplas.2022.103478
Received 28 June 2022; Received in revised form 25 October 2022;
Available online 9 November 2022

forms of Bauschinger effects and discuss potential mechanisms related to this extraordinary material behavior. Different microstructural models have been developed to explain the Bauschinger effect. Most importantly (i) Masing's model, which fundamentally addresses the role of residual stresses and "hard" and "soft" regions in polycrystalline materials (Masing, 1926); (ii) extensions of Masing's approach that consider inter- and intragranular residual stresses (Allain-Bonasso et al., 2012; Feaugas, 1999; Hu et al., 2017; Muhammad et al., 2017); (iii) models focusing on the interaction of dislocations created during initial deformation with precipitates, particles or other obstacles, such as grain boundaries or forest dislocations (Brown, 1977); (iv) mechanically inspired models describing the development of elastic back stresses (Abel and Muir, 1972; Hu et al., 2017; Kostryzhev, 2009; Kostryzhev et al., 2010; Lee et al., 2013; Liao et al., 2017; Plumtree and Abdel-Raouf, 2001; Richards et al., 2011; Sleeswyk and Kemerink, 1985; Stout and Rollett, 1990; Xue et al., 2016; Zhu et al., 2013); as well as (v) explicit microstructural models of the formation and decomposition of substructures due to annihilation (Bate and Wilson, 1986; Copreaux et al., 1993; Härtel et al., 2017; Hasegawa et al., 1975; Johnson et al., 1990; Lewandowska, 2003; Mughrabi, 1983; Peeters et al., 2002; Rauch, 1997; Rauch and Schmitt, 1989; Schmitt and Baudelet, 1985; van Riel and van den Boogaard, 2007; Vincze et al., 2005). This wealth of scientific literature clearly indicates the complex interaction of multiple microstructural and micromechanical phenomena that contribute to Bauschinger effects.

The present work builds on, and adds to, a previous study (Härtel et al., 2019) where Bauschinger effects in uniaxially deformed sheet metals of an interstitial-free (IF) DC06 steel were investigated both mechanically and microstructurally. Focus is now shifted from uniaxial loading to equi-biaxial tension-compression testing. It is worth mentioning that most experimental studies dealing with Bauschinger effects have so far been performed on bulk materials with conventional tensile and subsequent compression tests, or with shear tests with alternating shear directions. In contrast, the experimental work presented here considers in-plane loading of thin sheet materials (thickness < 1.5 mm), which is both of scientific and technological interest. While bulk materials can be tested mechanically in tension followed by compression without issues like buckling, similar experiments on sheet metals are considerably more difficult (Härtel et al., 2016; Kuwabara et al., 2001). Several approaches have been proposed to overcome this issue. In uniaxial experiments, various groups have reported experimental approaches where buckling is at least partially suppressed by the use of support plates or similar add-on structures (Boger et al., 2005; Härtel et al., 2017; Knoerr et al., 2013; Kuwabara et al., 2001; Lee et al., 2013; Piao et al., 2012; Tan et al., 1994). Much less work has been published on biaxial load cases. In order to investigate the low-cycle fatigue behavior of sheet metals, biaxial tension-compression-tests were performed by the group of Biermann (Ackermann et al., 2015, 2014; Kulawinski et al., 2017, 2014, 2011a, 2011b). No focus was placed on Bauschinger effects and applied (von Mises) strain amplitudes were below 1 %. Moreover, the sheet thickness in these experiments was higher than 6 mm, which considerably reduces buckling sensitivity. Conventional cruciform specimens (Hannon and Tiernan, 2008; Zhang et al., 2021) for biaxial tensile tests on thin sheet materials (Banabic et al., 2020; Bruschi et al., 2014; Xiao, 2019) are inappropriate for investigations on the biaxial Bauschinger effect because of their sensitivity to buckling under compression load. In Sofinowski et al. (2019) a combined experimental and crystal plasticity analysis of biaxial load path changes was performed using cruciform specimens with a reduced thickness in the measurement region. The sheet samples had a thickness of 10 mm to avoid buckling. No macroscopic stress data was recorded in the experiments.

Experimental methods dedicated to biaxial compression tests are rare (Bhaskar et al., 2021). The most common approach, layer compression testing, makes use of cylindrical samples where 10 or more coin-shaped thin sheet samples are stacked on top of each other and uniaxial compressive loading is equivalent to biaxial in-plane deformation (Barlat et al., 1997; Bruschi et al., 2014). Unfortunately, delamination of the samples during loading often occurs. To overcome this issue, Zillmann et al. developed an experimental setup that directly allows for biaxial, in-plane compression testing of thin sheet samples (Zillmann et al., 2015, 2014, 2011). To avoid buckling, a relatively small, square-shaped (4.2×4.2 mm^2) sample and a mechanical device that translates the horizontal movement created by a uniaxial testing machine into a biaxial vertical movement of four integrated plungers is used. The small sample can be machined out of larger cruciform specimens that have been pre-deformed in biaxial tension. This approach – combining biaxial tension of cruciform specimens, machining of smaller square-shaped samples, and subsequent testing in biaxial compression – forms the basis of our investigation of equi-biaxial Bauschinger effects in sheet metals, which is reported here for the first time. We performed equi-biaxial tensile tests with a cruciform specimen described in Schmaltz and Willner (2014, 2013), Zillmann et al., 2015) and subsequent equi-biaxial compression tests on an IF DC06 steel sheet[3]. Considering different maximum tensile strains, we characterize the magnitude of the resulting Bauschinger effects during compressive loading. In order to analyze the microstructural evolution during the different steps of plastic deformation, we study transmission electron microscopy (TEM), high-resolution electron back-scatter diffraction (HR-EBSD) and X-ray diffraction (XRD) results obtained from relevant deformation stages. Furthermore, we performed an in-situ neutron diffraction study on equi-biaxial tensile testing with a focus on the build-up of residual stresses. These results allow a detailed discussion of the contribution of the formation and decomposition (annihilation) of substructures, the development of elastic back stresses from the interaction of dislocations with other dislocations and grain boundaries, and particularly

[3] It is worth noting that, as pointed out by a diligent reviewer, from a continuum mechanical perspective, hydrostatic stress has no effect on plastic deformation in the sheet metal studied here. Then, equi-biaxial tension is indeed equivalent to uniaxial compression, and equi-biaxial compression is equivalent to uniaxial tension. This is, for instance, why layer compression tests are frequently used to experimentally characterize the onset of plastic deformation during equi-biaxial tension. One may therefore ask whether our experimental, equi-biaxial experiments cannot be simply substituted by their uniaxial counterparts: theoretically, uniaxial load reversal experiments should lead to identical changes of yield stresses and thus to exactly the same Bauschinger effects. However, (as our experimental results presented in the remainder of this paper clearly show), even minor amounts of mechanical anisotropy have a sufficiently strong effect on biaxial deformation to produce deviations from the theoretical results expected for isotropic materials. Therefore, actual biaxial experimental work is in fact useful to investigate Bauschinger effects under the more complex conditions studied here.

of compressive residual stresses that facilitate yielding under equi-biaxial compression.

2. Material and methods

2.1. Material

An interstitial-free DC06 steel sheet (0.02 wt.-% C, 0.25 wt.-% Mn and 0.3 wt.-% Ti and Nb) with a thickness of 1 mm was used in this study. Its mechanical behavior has already been characterized in some detail, (Clausmeyer et al., 2013; Güner et al., 2013; Härtel et al., 2019, 2016; Yin et al., 2014). The DC06 steel serves as a simple reference material because the low amount of alloying elements allows to exclude additional effects associated with impurities or the formation of precipitates (Jeong et al., 2015). In a previous study (Härtel et al., 2019), we microstructurally characterized the initial material condition; TEM analysis indicated that the as-received sheet material exhibits a low dislocation density. Dislocation density measurements based on EBSD data confirmed a relatively low value of $6 \cdot 10^{12}\ m^{-2}$ (Härtel et al., 2019).

2.2. Biaxial testing

In order to investigate Bauschinger effects associated with biaxial loading, we designed a novel experimental protocol: First, cruciform specimens, laser-cut from the steel sheets with a geometry as described in Schmaltz and Willner (2014, 2013), Zillmann et al. (2015) were subjected to equi-biaxial tensile loading up to different amounts of plastic strain. Each arm of the cruciform specimen has a width of 60 mm. All radii were optimized with the help of FE simulations to obtain a homogeneous biaxial strain distribution up to 3 % of engineering strains along each axis. The smallest cross section is 14.544 mm^2. After unloading, $4.2 \times 4.2\ mm^2$ square-shaped biaxial compression samples were machined by wire erosion (Zillmann et al., 2015) out of the inner part of the cruciform specimens. Fig. 1 shows a cruciform specimen with relevant dimensions and schematically indicates how the compression-sample is located with respect to the cruciform specimen's central region of homogeneous deformation.

The equi-biaxial tensile tests were performed with the help of a biaxial electromechanical tension and compression testing machine by Zwick/Roell. Each of the four drives is equipped with a load cell (20 kN). Both axes can be controlled separately. The determination of stress values in biaxial tensile specimens is not as straight-forward as in uniaxial tensile testing. Zillmann et al. performed several FE analyses using the distinct specimen geometry also used in the present study. They found that one can define an equivalent cross section for the equi-biaxial load case of 18.0 mm^2 (which significantly differs from the smallest cross section of 14.544 x 1 mm^2, see Fig. 1) to determine stress values from the measured force data; this approach was demonstrated to work very well for strains up to 2 %, (Zillmann et al., 2015). These results were also confirmed by more detailed investigations in Härtel et al. (2018). In the present paper, we consequently also used an equivalent cross section value of 18.0 mm^2 to determine the tensile stresses. Strain values were determined after the mechanical experiments with a digital image correlation (DIC) system (GOM, ARAMIS) (Härtel et al., 2018). We particularly analyzed separate stress-strain-curves for both (x and y) axes, where the x-axis was always in rolling direction (RD). All equi-biaxial tensile tests were performed with a displacement-controlled loading of 0.04 mm/s for both axes, which corresponds to a strain rate of 0.004 s^{-1}. Initially, several tests were performed up to failure of the specimens. In a post processing step with the ARAMIS software, strain-time diagrams were determined. Force-time diagrams were also determined from all load cells of each drive of the biaxial tensile machine. Both data sets were combined to derive force-strain diagrams, which provided as basis for the definition of

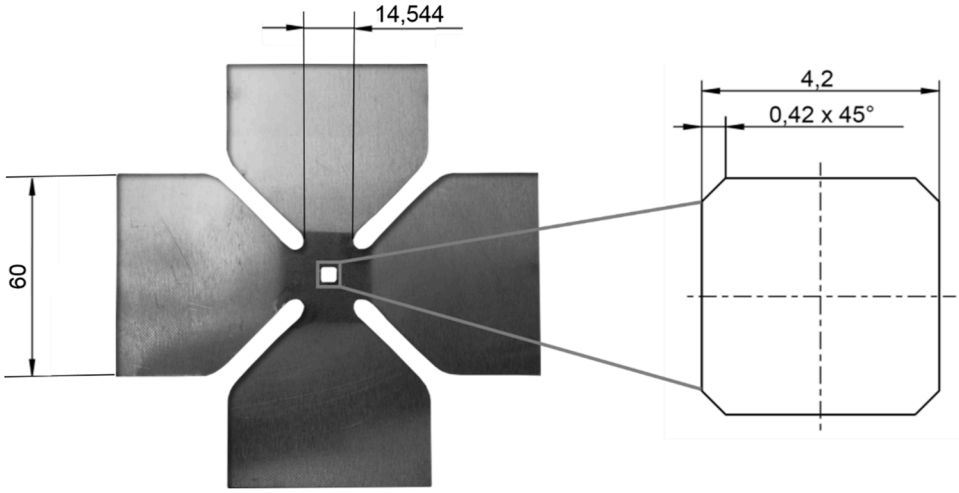

Fig. 1. Cruciform specimen (left), based on Schmaltz and Willner (2014, 2013), Zillmann et al., 2015) and biaxial compression specimen (right), (Zillmann et al., 2015). The cruciform specimens were deformed up to different maximum tensile strains (0.5 %, 1 %, 1.5 % and 2 %). For the subsequent biaxial compression tests, the compression specimens were machined out of the inner part of the cruciform specimens.

critical force values that were used in our later experiments to achieve relevant strains. Due to texture effects and different work hardening rates in RD and TD, the critical force values were not reached simultaneously; then forces acting along the "hard" axis (i.e., TD) were held constant until the "soft axis" also arrived at the critical force value. As this effect only occurred in the very final stages of loading, the predominant deformation type remained equi-biaxial. The equi-biaxial tensile specimens used for our detailed study of Bauschinger effects were deformed up to plastic strains of approximately 0.5 %, 1 %, 1.5 % and 2 %, respectively, along each axis.

The subsequent equi-biaxial compression tests were performed with the help of a servo-controlled Zwick/Roell UPM 1475 testing machine with the custom-designed setup for in-plane loading described in Zillmann et al. (2015). The forces were measured with the help of calibrated strain gages positioned on the four plungers. Strains were also recorded and analyzed with the GOM DIC system. Stress values were calculated from force data recorded during the experiments following a correlation procedure that was developed for DC06 and that is outlined in Zillmann et al. (2015). Similar to the equi-biaxial tensile tests, we analyzed the stress-strain-curves for the x- and y-axis separately, with the x-axis always in RD. The crosshead velocity of the testing machine was set to 0.018 mm/s. This also corresponds to an in-plane strain rate of 0.004 s^{-1}. The design of the specialized biaxial compression testing setup limits plastic deformation up to about 5 % (Zillmann et al., 2015). This strain range is of a similar order of magnitude as the previously applied tensile strains and was found to be sufficient for the present study. Further details, especially on the very high accuracy of the DIC strain measurements, on both the equi-biaxial tensile and equi-biaxial compression setup are described in detail in Zillmann et al. (2015).

Complementary equi-biaxial tensile tests with concurrent neutron diffraction measurements were performed with our cruciform specimens (see Fig. 1) at the Paul-Scherrer-Institute (PSI) using the POLDI neutron strain scanner (Repper et al., 2013; Stuhr, 2005; Stuhr et al., 2005). While the setup and the testing parameters were similar to the methods described in Repper et al. (2013); Sofinowski et al., 2019; Van Petegem et al., 2016), our specimen geometry differed from the cruciform samples used in previous in-situ diffraction work at PSI. The biaxial tensile test rig at PSI is identical to the one used in our previously described biaxial tensile experiments (Van Petegem et al., 2016). The tests were also displacement-controlled with a comparable strain rate of 0.005 s^{-1}. In the elastic regime, the tests were stopped in load steps of 400 N. After a hold-time of 1 min for stress relaxation, the shutter of the neutron source was opened and neutrons illuminated the specimen on an area of 3.8 × 3.8 mm^2 (which, incidentally, is very close to the size of our biaxial compression specimen). After a sufficient time of neutron illuminating the shutter was closed and the equi-biaxial deformation was continued. In the elastic-plastic regime, measurements were performed in load steps of 200 N until a macroscopic strain of approximately 2 % in RD (x-axis) was reached. During unloading, measurements were also performed in steps of 400 N as well as in the final, unloaded state at the end of the experiment. Post processing of the diffraction data was accomplished using the methods described in Van Petegem et al. (2016).

2.3. Microstructural analysis

For microstructural analysis of the equi-biaxial Bauschinger effect in DC06, samples for electron microscopy and XRD were investigated at different stages of plastic deformation. Comparable to the pioneering work of Hasegawa et al. (1975) and our own recent study (Härtel et al., 2019), the first set of samples was taken from the cruciform specimens after unloading from different maximum tensile strains (0.5 % and 2.0 %); a second set of samples was taken immediately after the load reversal (yielding under biaxial compression); a final set was analyzed after plastic strains of about 3.5 % in equi-biaxial compression.

All specimens were prepared for TEM investigations by mechanical grinding and thinning followed by electro-polishing: First, the 1 mm thick specimens were mechanically wet grinded to 100 μm with coarse sand paper. After that, a round slice of 3 mm diameter with a mark to indicate the rolling direction was stamped out. Then, we used a Tenupol-5 Doublejet for electrolytically thinning the sample from both sides with electrolyte A7 from Struers at a temperature of -33 °C and a voltage of 28 V. Thinning was continued until the foil was perforated. Artefacts were further removed using an Ar-ion beam with 3 kV acceleration voltage. This electrolytic thinning procedure avoids the impact of preparation on the TEM foils. TEM analysis was performed with a Hitachi H8100 TEM at an accelerating voltage of 200 kV. EBSD measurements were performed on the same TEM foils using a TESCAN MIRA3 SEM with an accelerating voltage of 20 kV. Focussing on substructures, we analyzed areas of about 25 × 60 μm^2 (step size 75 nm). Moreover, geometrically necessary dislocation (GND) density was calculated from EBSD data (using a step size of 1 μm on areas of 50 × 100 μm^2) by pattern cross correlation (Littlewood et al., 2011; Wilkinson et al., 2006) with the software package CrossCourt™ (CrossCourt EBSD Strain Mapping Software, BLG Productions Ltd., UK, www.blgproductions.co.uk), based on methods described in Hughes et al. (2003), Pantleon (2008), Ruggles and Fullwood (2013), Wilkinson et al. (2006), Wright et al. (2011).

We performed XRD measurements (Co-K_α; accelerating voltage 35 kV) in an X-ray diffraction device (D5000 by Siemens) on areas of 2 × 2 mm^2 on the cruciform specimens as well as on the biaxial compression specimens prior to preparation of the TEM samples. In all measurements, the samples were oriented such that the RD was parallel to the XRD system's x-direction and TD was parallel to the y-direction. For further details on the XRD setup see (Mehner et al., 2018). Stress states were analyzed based on the $\sin^2\psi$-method (Güner et al., 2013). Finally, we note that no significant change of texture could be detected by XRD after loading[4], which agrees well with the small accumulated plastic strains (6 % or less in all experiments); texture evolution therefore is not considered in the present paper.

[4] To document the absence of any texture changes, we present orientation distribution function (ODF) plots of the initial state, of the material after 2 % equi-biaxial tensile straining, and after additional 3.5 % equi-biaxial compression loading as Supplementary Material.

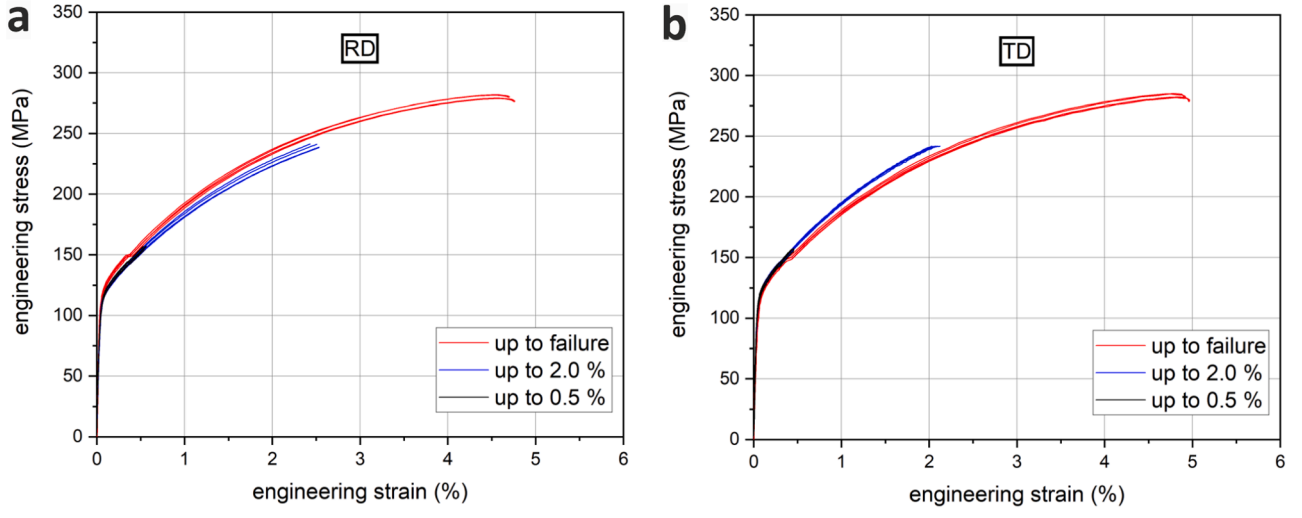

Fig. 2. Engineering stress-strain curves of biaxial tensile tests up to failure and up to 0.5 % as well as 2 % maximum tensile strain. The parameter for stopping at those strain levels were determined from the tests up to failure and were considering force values as hard ends.

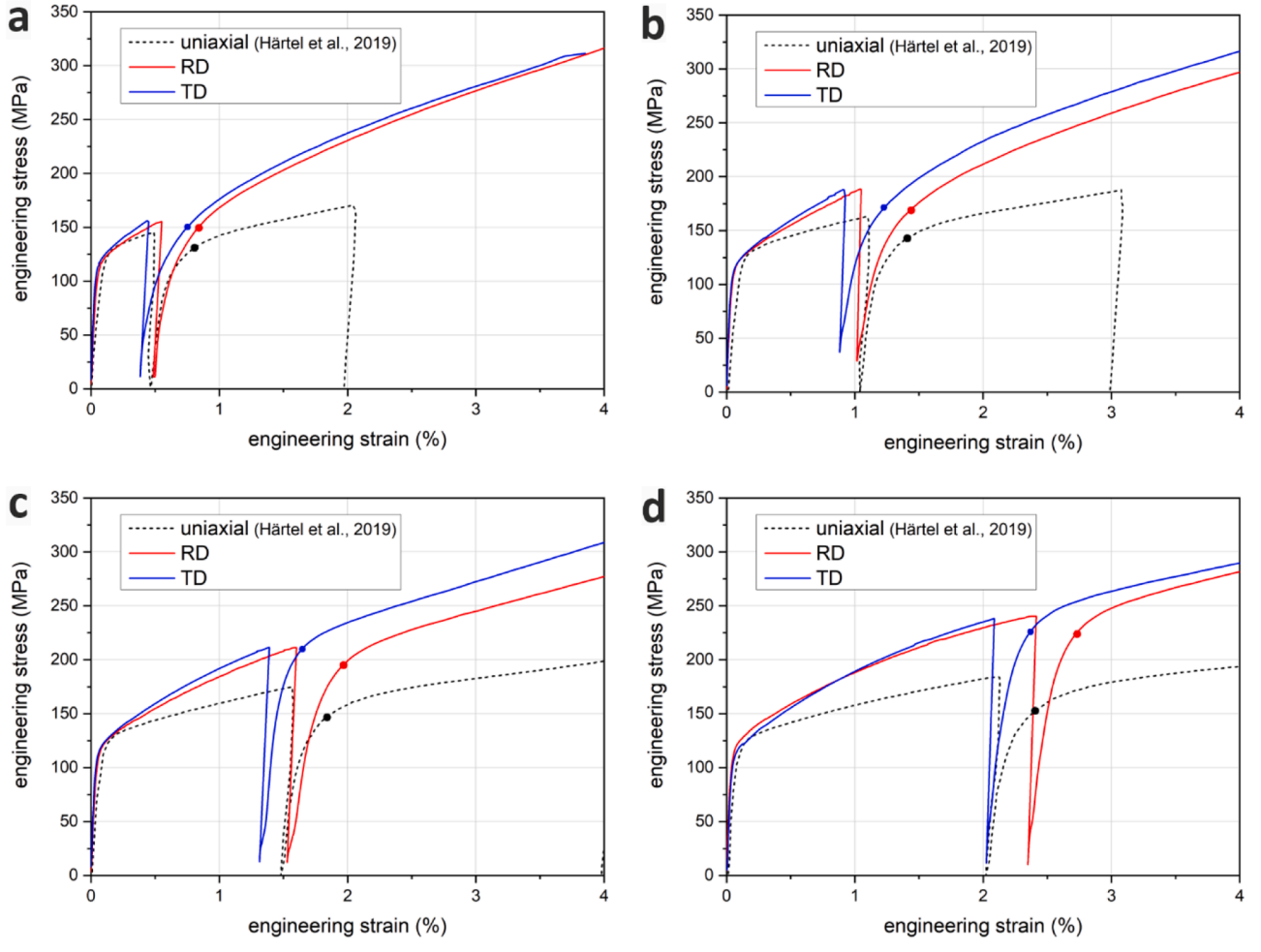

Fig. 3. Engineering stress-strain-curves of equi-biaxial tensile tests and subsequent equi-biaxial compression tests (numerical values correspond to measurements on each axis, i.e., in RD and TD, respectively). Biaxial tensile loading was performed up to different maximum tensile strains (approx. 0.5 %, 1 %, 1.5 % and 2 %). The data associated with compressive loading is given in absolute values, both for stresses and strains. Two dots in each plot indicate the 0.2 % yield point after load reversal. All conditions clearly exhibit a decrease in yield strength after load reversal.

3. Results and discussion

3.1. Mechanical quantification of biaxial Bauschinger effects

In Fig. 2, the results from five equi-biaxial tensile tests each, up to failure, to 0.5 % and 2 % maximum tensile strain for RD and TD direction are shown. Note that stress values of individual biaxial tensile experiments differed by less than a few MPa in all cases considered here. This demonstrates the satisfactory reproducibility of our experiments despite some experimental scatter. We first performed five equi-biaxial tensile tests until failure of the cruciform specimens. The force and displacement values of the biaxial tensile testing machine were obtained directly and in real time. The strain distributions were captured with 3D-DIC and required a subsequent calculation and analysis of the strain fields. So, real time strain values could not be used directly to control our biaxial experiments. Instead, the stopping points for all equi-biaxial tensile tests with different maximum tensile strains were determined from the average force-values of the force-strain curves determined from the five initial equi-biaxial tensile tests until failure in RD. The resulting strains were again determined after testing. The corresponding strain values of approximately 0.5 %, 1 %, 1.5 % and 2 % are used in the remainder of this paper as qualitative strain measures despite some experimental deviations.

All stopped equi-biaxial tensile tests were subsequently followed by equi-biaxial compression tests. In Fig. 3, the results of mechanical testing are summarized as engineering stress-strain curves (both stress and strain values correspond to the uniaxial measurements on each axis). All curves result from an averaging procedure from a total of five experiments performed under identical conditions. In all plots, absolute values were used for both stress and strain data measured in the subsequent equi-biaxial compression stage of our experiments. This allows to directly compare maximum tensile stresses prior to unloading with the subsequent onset of plastic deformation during equi-biaxial compression. For a visual comparison, we also added the values of the uniaxial tension-compression tests of the identical material from our recent study (Härtel et al., 2019).

At first, all specimens were deformed in equi-biaxial tension up to different maximum strains (approx. 0.5 %, 1 %, 1.5 % and 2 %). In all equi-biaxial tensile tests, initial yielding occurred at very similar stress levels, and work hardening rates were also very similar. The work hardening rate in TD was slightly higher compared to that of RD, which is related to texture. This effect also leads to minor, but systematic differences between RD and TD in terms of the maximum tensile strains in our experiments, with strains in RD always exceeding those of TD. The stress-strain curves in Fig. 3 also include the elastic unloading part after equi-biaxial tension. The subsequent equi-biaxial compression tests were performed up to strains of 3.5 % along each axis. The hardening behavior in equi-biaxial compression also slightly differs between RD and TD. We note that, in Fig. 3, the apparent Young's modulus in equi-biaxial compression appears to be somewhat lower, which is related to a different compliance of our biaxial compression testing setup. Experiments with load reversal are often characterized by reverse flow curves that exhibit a well-rounded region, which obscures the renewed onset of yielding. This effect is also observed in Fig. 3. Similar to the approach proposed in Tan et al. (1994), we therefore applied a 0.2 % offset yield point criterion as indicated by dots in Fig. 2. To facilitate this approach, the linear-elastic slope was approximated by fitting a linear function to stress-strain data between 50 and 100 MPa in each curve.

For the 0.5 % maximum tensile strain condition, the maximum stress under equi-biaxial tension (i.e., prior to unloading) is 157 MPa, and subsequent yielding under equi-biaxial compression commences at about 151 MPa; both stress values are the same for RD and TD, respectively. In the case of 1 % tensile strain, the maximum stress is 188 MPa, and yielding under equi-biaxial compression begins at 171 MPa, again for both RD and TD. After 1.5 % the maximum stress under equi-biaxial tension is 213 MPa and yielding under equi-biaxial compression is at 208 MPa for RD, and 196 MPa for TD. This is the only condition where stress values in biaxial compression differ markedly between RD and TD and especially the yielding in RD exhibits large deviations. For the 2 % condition, the maximum stress under equi-biaxial tension is 241 MPa and yielding under equi-biaxial compression begins at 223 MPa. All experimental data presented in Fig. 3 clearly document the occurrence of a Bauschinger effect during biaxial loading/ load reversal. We highlight that our use of the 0.2 %-yield criterion is conservative in the sense that the onset of yielding in compression actually already occurs at lower stresses, which can be translated to an even more pronounced Bauschinger effect.

Uniaxial tension-compression tests on the same material and using similar maximum tensile strains were already reported in Härtel et al. (2019). These results were also in good agreement with similar studies on low-alloyed bulk steel materials (Gupta and Kodali, 1976; Richards et al., 2011). In the more conventional, uniaxial experiments, the DC06 steel sheet exhibits higher differences between the maximum stress under tensile load and the 0.2 % yield point under compression. To quantitatively compare effect sizes, we consider the so-called Bauschinger effect factor α, which is defined as the ratio between the (compressive) yield strength after load reversal, σ_C and the previous maximum (tensile) stress, σ_T: $\alpha = \sigma_C/\sigma_T$, (Gupta and Kodali, 1976; Richards et al., 2011). In the absence of a Bauschinger effect, $\alpha = 1$; increasing deviations from 1 indicate a more pronounced Bauschinger effect. Fig. 4 shows α-values determined from our equi-biaxial experiments (separately for RD and TD) as well as from our previous uniaxial study (Härtel et al., 2019). Error bars correspond to standard deviations after averaging 4 data sets for each material condition. Even at relatively low tensile strains (0.5 %), the α-values demonstrate the presence of Bauschinger effects. With increasing maximum tensile strain, this effect clearly becomes more pronounced, with α-values decreasing to approx. 0.91 in all cases. The only marked deviation occurs for strains of 1.5 % (RD), which is most likely related to the larger scatter already observed in Fig. 3. Interestingly, in the case of highest tensile strains, the uniaxial data differs from the equi-biaxial results: While α continues to decrease during uniaxial loading, both RD and TD data in the equi-biaxial experiments indicate a reduced Bauschinger effect – despite the fact that the biaxial experiments are characterized by larger equivalent plastic strains than the uniaxial ones. To summarize our basic mechanical observations, both the stress-strain data and the corresponding α-values show that Bauschinger effects occur in equi-biaxial load cases, and that they can distinctly differ from uniaxial load cases: While equi-biaxial Bauschinger effect factors quickly saturate, the uniaxial Bauschinger effect Factors continuously decrease in the strain range studied here.

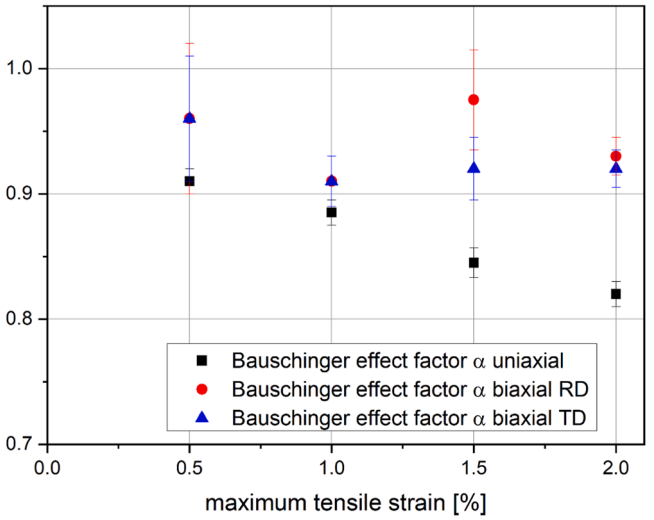

Fig. 4. Bauschinger effect parameter α as a function of maximum tensile strain for equi-biaxial loading (both in RD and TD) as well as for uniaxial loading, (Härtel et al., 2019). Deviations from $\alpha = 1$ correspond to the occurrence of Bauschinger effects.

3.2. Qualitative assessment of the microstructural evolution during the different stages of biaxial tension-compression loading

In order to analyze the microstructural changes related to Bauschinger effects, we performed TEM investigations on samples taken at different stages of our equi-biaxial tension-compression tests. Figs. 5 and 6 represent the two extreme cases with low (0.5 %) vs. high (2 %) maximum tensile strains, respectively. In both figures, we present characteristic TEM bright field images that correspond to the microstructures at maximum tensile strain (a), the stress immediately after yielding under equi-biaxial compression (b), and after plastic straining up to 3.5 % in equi-biaxial compression (c). These characteristic conditions are further indicated in the corresponding stress-strain curves shown in Figs. 5d and 6d. The orientation of the samples for all bright field images corresponds to that indicated by arrows in Fig. 5a. Considering the first case (Fig. 5, maximum tensile strain of 0.5 %), we observe a slight increase of dislocation density compared to the undeformed, initial material (see Fig. 1a in Härtel et al. (2019)) but without the formation of any substructures such as dislocation cells. Compared to the microstructure after uniaxial loading up to similar strains (Härtel et al., 2019), the dislocation density appears slightly increased. Of course, the dislocation density differs between different grains: for instance, the dislocation density in the grain on the upper left is quite low while in the grain below it is slightly higher. We emphasize that, while this interpretation is qualitative in nature, observations under different tilt angles did not lead to any different impressions. Clearly, already after small amounts of tensile plastic straining, different dislocation densities can be documented in different grains, and this may lead to varying local yield stresses. Moreover, this indicates that intergranular residual stresses as well as geometrically necessary dislocations may occur in the vicinity of grain boundaries to compensate different amounts of grain shape deformation (Gao and Huang, 2003) and hence preserve compatibility at the grain boundaries (Härtel et al., 2019).

After load reversal, immediately after yielding under equi-biaxial compression (see Fig. 5b, which again shows a representative example of a larger number of observations using different tilt angles in the TEM), the dislocation density is decreasing in the vicinity of grain boundaries. Such a difference in local dislocation density in individual grains as well as a variation when comparing different grains have been related to the macroscopic Bauschinger effect (Feaugas, 1999; Härtel et al., 2019; Hu et al., 2017). As expected, continued compression up to a larger strain of 3.5 % leads to further increased dislocation densities and to a pronounced formation of substructures (dislocation walls) that are typically formed to reduce strain energy (Hasegawa et al., 1975; Lewandowska, 2003), Fig. 5c. The observed evolution of dislocation density is in line with earlier reports, e.g. by Hasegawa and Yakou who reported similar results in uniaxial tension-compression tests on pure aluminum (Hasegawa et al., 1975). For our DC06 sheet material, however, we previously observed slightly different trends under uniaxial loading, where the dislocation density was further increased after the load path change. Furthermore, after comparable deformation under uniaxial compressive load, the formation of substructures just began and was not as pronounced as in the equi-biaxial load case considered here (Fig. 5c).

In Fig. 6, TEM micrographs of representative microstructures at the three different stages of equi-biaxial tension-compression deformation with a maximum equi-biaxial tensile strain of 2 % are shown. At the maximum equi-biaxial tensile strain of 2 % (Fig. 6a), the increased dislocation density already leads to the pronounced formation of substructures (dislocation cells) in the vicinity of the grain boundaries, accompanied by the onset of substructure formation in the grain interiors. The presence of some regions with a higher dislocation density adjacent to regions with lower dislocation density may produce intragranular residual stresses, (Feaugas, 1999; Hu et al., 2017; Muhammad et al., 2017). Compared to our microstructural observations under uniaxial loading up to 2 % (Härtel et al., 2019), the dislocation density appears much higher and the dislocation substructures (dislocation walls) are more pronounced after 2 % of equi-biaxial tensile deformation.

The load path change (b) again leads to a decreased dislocation density, Fig. 6b. Especially in the vicinity of the grain boundaries, a

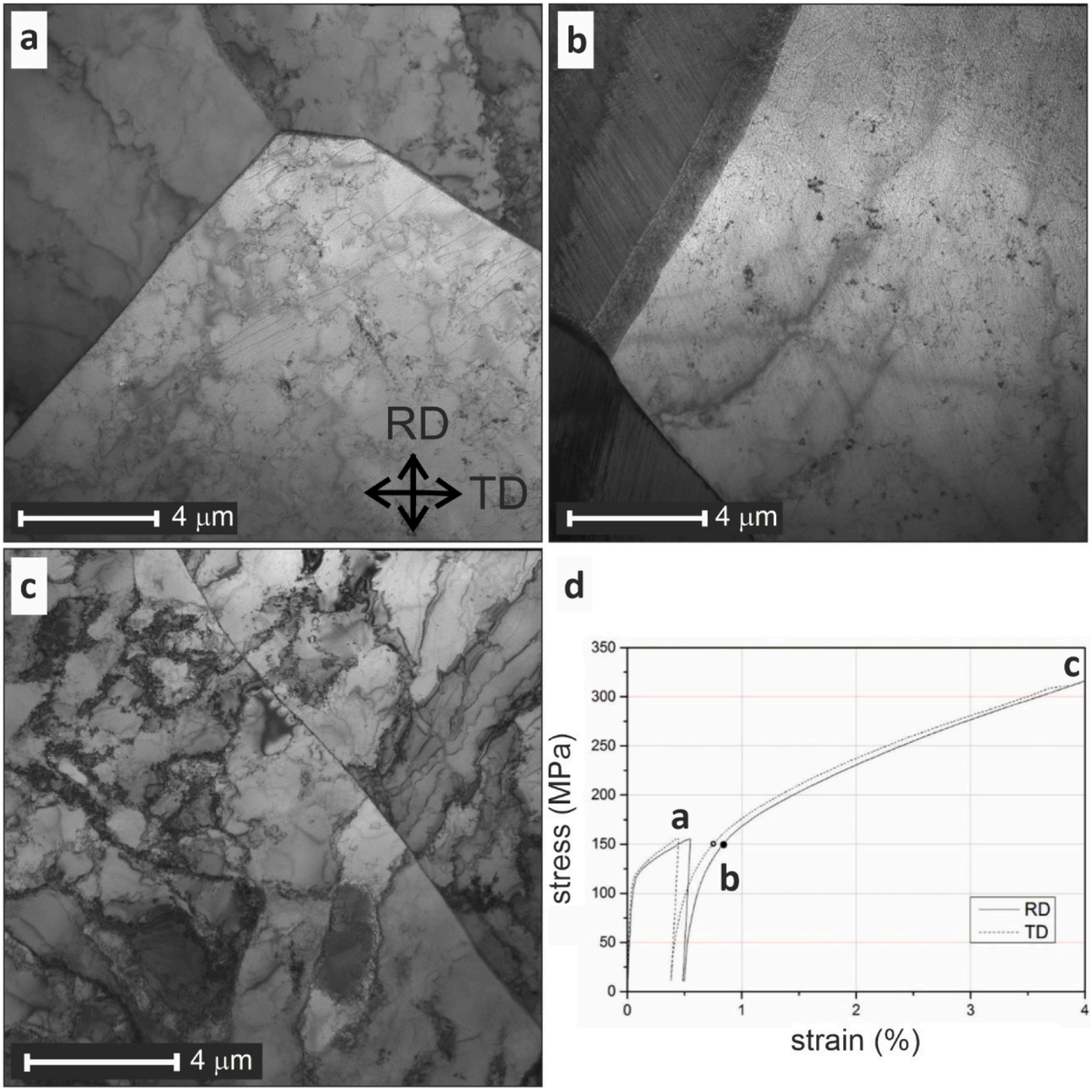

Fig. 5. Characteristic TEM bright field micrograhps at different stages of the equi-biaxial tension-compression test (maximum biaxial tensile strain: 0.5 %). (a) Loading to the maximum equi-biaxial tensile strain, leads to a slightly increased dislocation density compared to the initial condition. b) Some decrease can be detected after load reversal in the vicinity of the grain boundaries. (c) After reaching a compressive equi-biaxial strain of 3.5 %, substructures (dislocation cells) are formed. (d) The different stages of deformation related to (a)–(c) are highlighted in the stress-strain curves for RD and TD.

decomposition of some substructures by annihilation can be observed. Nevertheless, substructures are not fully annihilated and some remain, especially in the grain interiors. This process again can lead to increasing intergranular residual stresses. In addition, we observe a difference in dislocation density in different grains, which may lead to intragranular residual stresses (Feaugas, 1999; Härtel et al., 2019; Hu et al., 2017; Muhammad et al., 2017). An annihilation of substructures was also observed in Hasegawa et al. (1975) and may contribute to the macroscopic Bauschinger effect. The final load stage, equi-biaxial compression up to 3.5 %, leads to a renewed formation of substructures (dislocation walls and cells), which is commonly believed to reduce strain energy (Hasegawa et al., 1975; Lewandowska, 2003; Vincze et al., 2005), Fig. 5c. During uniaxial deformation, those substructures are less pronounced (Härtel et al., 2019), which might be related to the assumption that a larger number of slip systems can be activated during multi-axial loading and

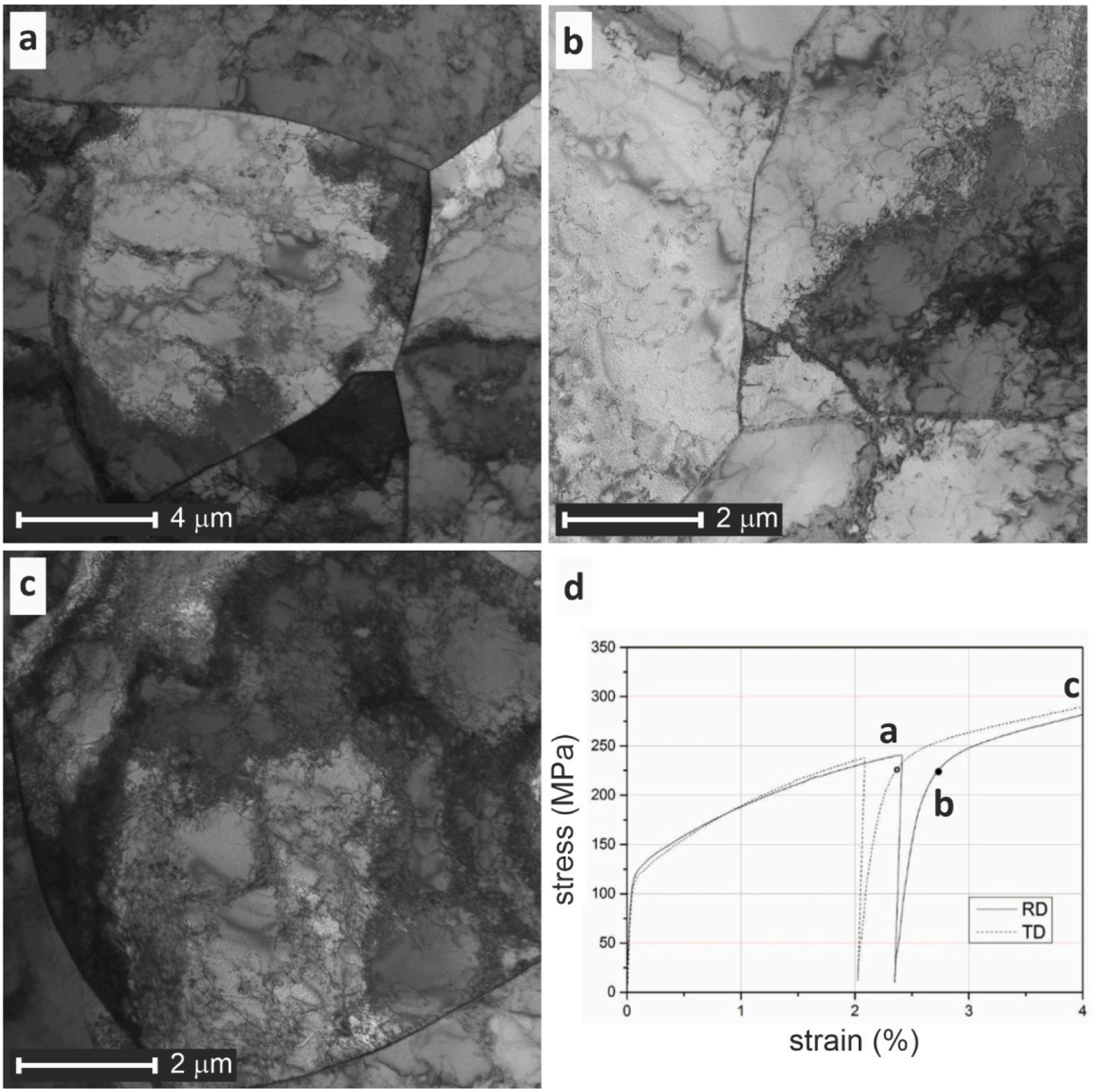

Fig. 6. TEM bright field micrographs of the DC06 sheet material at different stages of the equi-biaxial tension-compression test (maximum equi-biaxial tensile strain: 2 %): (a) Increased dislocation density and dislocation cell formation in the vicinity of grain boundaries after loading to the maximum equi-biaxial tensile stress. (b) After load reversal, decreased dislocation density and decomposition of dislocation cells, especially near the grain boundaries, are observed. (c) With further equi-biaxial loading up to a strain of 3.5 %, the formation of new dislocation cells is again observed, (d) Different stages of biaxial deformation in the stress-strain curves for RD and TD as related to (a)–(c).

an increase of dislocation interaction mechanisms facilitates the formation of substructures (Laukonis and Ghosh, 1978; Mulder et al., 2015).

3.3. Detailed EBSD analysis of substructure formation and GND density evolution

While the TEM results presented above provide qualitative information on the development of dislocation substructures and the evolution of dislocation density values, a more quantitative view can be obtained by considering the HR-EBSD measurements performed on the same TEM samples. In Figs. 7a–c and 8a–c we present orientation maps (OM, on the left of each image) and third-order kernel average misorientation (KAM, on the right of each image) data for the same region. The CrossCourt™ software uses information

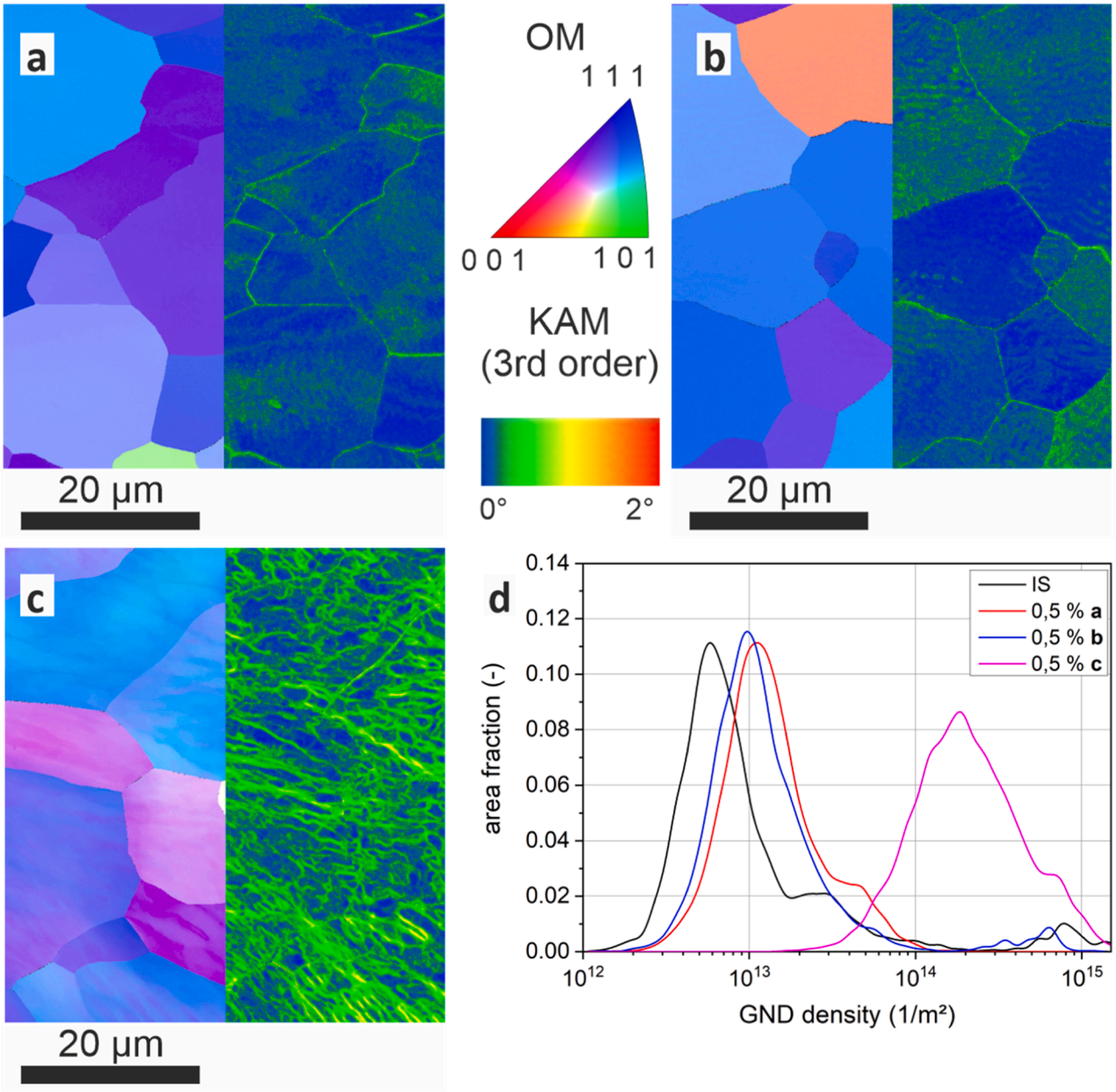

Fig. 7. Orientation maps (left parts of (a)–(c)) vs. kernel average misorientation maps (right parts of (a)–(c)) at different equi-biaxial load stages (maximum equi-biaxial tensile strain: 0.5 %). (a) After tensile loading, an increase in dislocation density and differences in local intergranular misorientations occur. (b) After the load path change, some grains with increased, relatively homogeneous KAM values are observed while other grains exhibit a strongly decreased local misorientation. (c) At a macroscopic strain of 3.5 % in equi-biaxial compression, substructures can be observed. (d) GND density distributions for the initial material and the three relevant conditions. Equi-biaxial tensile loading first increases the GND density. Subsequent load reversal leads to slight decrease. Further equi-biaxial compression finally results in a strong increase.

up to third next neighbors to determine local misorientation values. In addition, the Nye tensor description (Nye, 1953) was used to estimate the local GND density values, see also (Härtel et al., 2019). The corresponding GND density data are shown as a function of area fraction for the initial state of the material (IS) and for the three deformation states (corresponding to points a, b, and c in Figs. 5 and 6, respectively) in Figs. 7d and 8d.

The OM associated with tensile loading up to 0.5 % (Fig. 7a) reveals no evidence for the formation of substructures. Only different orientations in different grains can be observed, which agrees well with our TEM observations, Fig. 5a. However, the corresponding KAM data indicates a slightly increased level of local misorientations in some of the grains. While, in general, misorientations are observed in entire individual grains, they are especially pronounced near grain boundaries. Even during the very early stages of plastic deformation, dislocations pile up near grain boundaries, which results in locally increased dislocation densities as well as

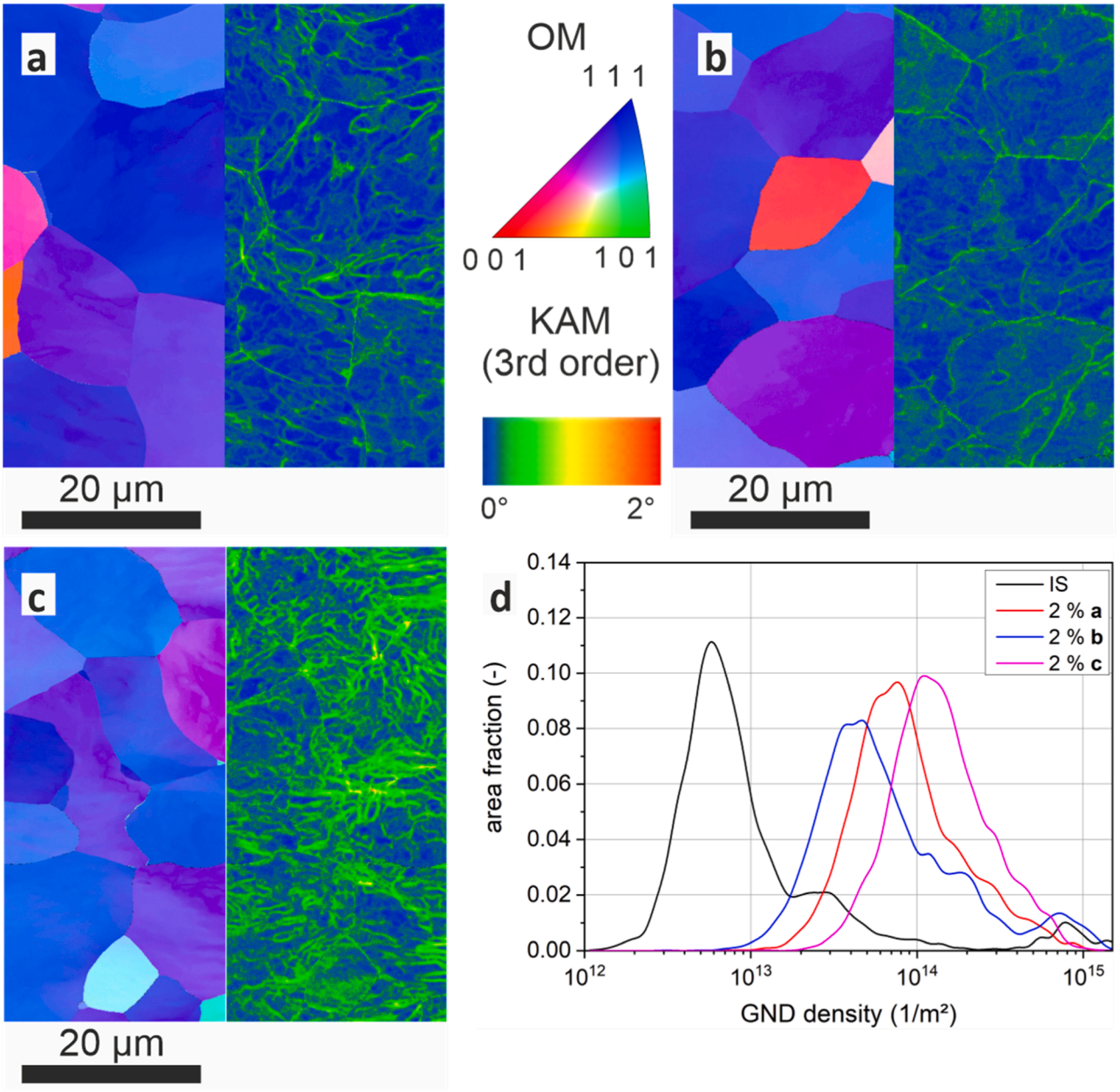

Fig. 8. Orientation maps (left in (a)–(c)) and KAM maps (right in (a)–(c)) at different stages of the equi-biaxial tension-compression test (maximum equi-biaxial tensile strain: 2.0 %). (a) After loading to the maximum equi-biaxial tensile strain, we observe the onset of substructure formation, with misorientations between different grains that can result in intergranular residual stresses. (b) Yielding in subsequent compression results in the decomposition of most of the substructures, leading to grains with relatively homogeneous KAM values and to an overall decreased GND density. (c) At a macroscopic strain of 3.5 % in equi-biaxial compression, we observe the renewed formation of substructures. (d) Corresponding GND density distributions.

misorientation. Piled-up dislocations can also lead to back stresses when the macroscopic load (and the corresponding, microscopic shear stress) are removed during unloading. In this material condition, relevant differences in misorientation are only developing on an inter-granular level, but they are not yet pronounced inside individual grains. Nevertheless, it is worth noting that even minor misorientations between different grains can in principle lead to intergranular residual stresses (Härtel et al., 2019) that are likely to contribute to the Bauschinger effects observed in the present study. As a first-order approximation, we consider only the peak value of the GND density ($1.3 \cdot 10^{13}\ m^{-2}$, Fig. 7d) to quantitatively compare dislocation density values (see also (Härtel et al., 2019; Wright et al., 2011)). As in our previous study on uniaxial Bauschinger effects (Härtel et al., 2019), we do not further analyze additional fluctuations in the GND density distributions. In comparison to the IS, the relatively small tensile deformation (0.5 %) already more than doubles the (average) GND density. Moreover, the GND density peak value is higher by about 30 % compared to that associated

with a similar uniaxial deformation, (Härtel et al., 2019).

After early yielding under equi-biaxial compressive load (Fig. 7b), we observe a distinct decrease in terms of misorientation in some grains, while other grains exhibit comparable and homogeneously distributed KAM values similar to those in Fig. 7a. In some grains, dislocation annihilation is likely to have occured, which in turn decreases misorientation. In other grains, additional plastic slip has been triggered and a balance between annihilation and newly arising local misorientation can be observed. The global GND density of this condition has an estimated peak value of $9.5 \cdot 10^{12}\ m^{-2}$. It is therefore decreased compared to the state at maximum biaxial tensile strain. This is in good agreement with our TEM results and confirms that dislocation annihilation processes take place, even though this effect is not as pronounced as reported in Hasegawa et al. (1975). Under uniaxial loading, also grains with high misorientation and grains with lower misorientation were observed, but overall the dislocation density increases, which has been related to the activation of dislocation sources and the subsequent interaction on different slip systems, (Härtel et al., 2019).

Finally, equi-biaxial compression to a strain of 3.5 % (Fig. 7c) results in the formation of distinct substructures in the grains, which is evident both from the OM and the KAM plots and which is also in good agreement with our TEM observations (Fig. 5). The misorientation distribution appears to become more heterogeneous in individual grains: While regions with very low misorientations are observed, they are surrounded by neighboring regions with considerably higher misorientation. The GND density is strongly increased to an estimated value of $1.8 \cdot 10^{14}\ m^{-2}$, Fig. 6d. The formation of substructures of the comparable uniaxially deformed material state is less pronounced (Härtel et al., 2019), with an estimated GND density that is one decade lower ($1.8 \cdot 10^{13}\ m^{-2}$, (Härtel et al., 2019)), which again emphasizes that biaxial deformation results in higher dislocation densities.

Considering loading up to 2 % of equi-biaxial tensile strain, Fig. 8a, we can already observe orientation differences related to the early development of substructures. This is also indicated by the KAM data that shows misorientation differences in the interior of individual grains as well as between different grains (which can lead to intragranular and intergranular residual stresses (Feaugas, 1999)). In comparison to the material states (i) at 0.5 % maximum equi-biaxial tensile strain (GND density $1.3 \cdot 10^{13}\ m^{-2}$, Fig. 7d), and (ii) at 2.0 % maximum uniaxial tensile strain (GND density $2.7 \cdot 10^{13}\ m^{-2}$, (Härtel et al., 2019)), the GND density is much higher, with a peak value of $7.9 \cdot 10^{13}\ m^{-2}$, Fig. 8d.

After the subsequent yielding under equi-biaxial compressive load (Fig. 8b), we observe a decomposition of the previously developed substructures. Neither in the OM nor in the KAM plot, substructures such as in Fig. 8a can be seen. Moreover, relatively homogeneous KAM values in every grain and an overall decreased misorientation occur. The observation of relatively constant KAM values in every grain is in contrast to the observations from 0.5 % maximum equi-biaxial tensile strain, where in some grains the GNDs were annihilated and misorientation values became almost zero, Fig. 7b. Fig. 8b instead indicates the decomposition of the substructures and no pronounced annihilation. That is why the estimated GND density is substantially decreased to $4.6 \cdot 10^{13} m^{-2}$, Fig. 8d.

Equi-biaxial compression up to strains of 3.5 % (Fig. 8c) leads to clearly visible substructures in all grains which is evident from the OM as well as the KAM plots. The estimated GND density is increased to a peak value of $1.2 \cdot 10^{14}\ \mathrm{m}^{-2}$, Fig. 8d, which is slightly reduced (but of the same order of magnitude) compared to the GND density for 0.5 % equi-biaxial tensile and subsequent 3.5 % equi-biaxial compressive strains. Compared to uniaxial deformation, the formation of substructures in the OM as well as the KAM plot is much more pronounced in biaxial deformation (Härtel et al., 2019). The estimated GND density for a comparable uniaxial deformation is only 35 %$(4.2 \cdot 10^{13}\ \mathrm{m}^{-2})$ (Härtel et al., 2019) of the equi-biaxial one.

We highlight that the quantitative HR-EBSD results discussed above are fully in line with the TEM results presented in Section 3.2. A comparison of microstructures in samples deformed up to 0.5 % versus 2 % equi-biaxial tensile strain indicates increased dislocation density values at maximum (equi-biaxial) tensile strain, particularly in the 2 % condition. Furthermore, our GND data clearly suggests a systematic evolution of dislocation density that can be directly related to the different loading stages. Generally, higher maximum tensile strains appear to lead to larger fluctuations of dislocation density values inside individual grains. While dislocation pile-ups can be formed near grain boundaries in both conditions, this effect is more pronounced at higher strains. Furthermore, load path changes are associated with annihilation processes. In addition, dislocation-grain boundary interactions may lead to back stresses that are likely to affect the biaxial Bauschinger effects observed in the present study.

3.4. Evolution of residual stresses

Our microstructural analyses demonstrate that residual stresses are likely to be built up during equi-biaxial tension-compression deformation, and to contribute to the macroscopic (biaxial) Bauschinger effects reported here for the first time. It is important to differentiate between residual stresses on the micro-scale (which are associated with strain gradients and result from the local microstructural deformation mechanisms discussed above) and long-range, macro-scale residual stresses that are built up in the entire sample as a consequence of plastic deformation. The latter, when integrated over the entire sample volume in a load-free condition, must cancel each other out; nevertheless, locally, macroscopic residual stresses can of course also affect the onset of yielding and thus affect the Bauschinger effects studied here. The samples used in the present study – cruciform-shaped for biaxial tension and square-shaped for subsequent biaixial compression – have each been carefully validated in previous studies (Härtel et al., 2018; Schmaltz and Willner, 2014, 2013; Zillmann et al., 2015, 2014, 2011). It was demonstrated by Finite Element Analysis, by Digital Image Correlation measurements and by subsequent analysis of displacement fields that the deformation (i.e., strain fields) in the center parts of the samples are homogeneous up to (and somewhat beyond) the strain levels used in the present study; strain gradients are negligible and they naturally predominantly occur in the arms of the cruciform specimen (and because of friction, near the edges of the compression specimen). In terms of proper validation, our samples therefore compare well with alternative approaches that have used similarly rigorous validation procedures such as (Deng et al., 2015; Hanabusa et al., 2013; Ogihara et al., 2020). We must however highlight that

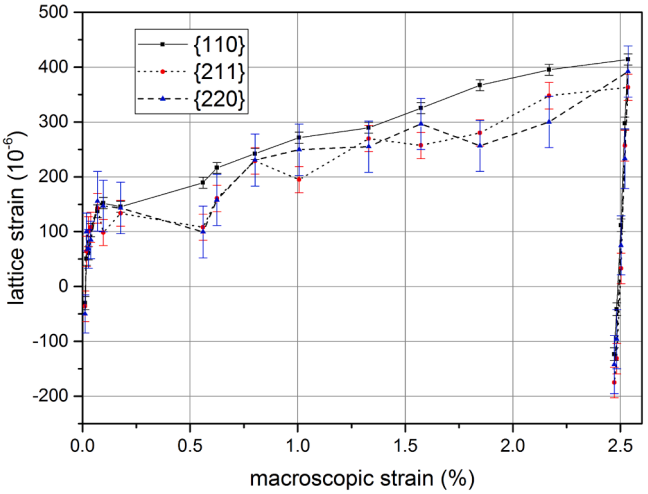

Fig. 9. Lattice strain values for the three grain families with the most diffracted neutrons as a function of the macroscopic strain in RD. All curves exhibit a similar shape: starting with negative lattice strains, an elastic slope is followed by an increase in lattice strain during work hardening, and the maximum lattice strain occurs at the maximum macroscopic tensile strain. Load removal leads to a decrease in lattice strain values and finally to compressive lattice at zero load.

in all of these studies, the focus was placed on strain homogeneity during (forward) loading itself and that the evolution of (elastic) strains during later unloading was typically not analyzed in detail. Unloading is likely result in some load transfer between different parts particularly of the cruciform sample and this may lead to residual stresses despite the excellent sample properties documented by previous validation experiments. Analyzing the build-up of (macro-scale) residual stresses therefore is important to fully understand the different factors influencing Bauschinger effects during equi-biaxial experiments.

Keeping these fundamental aspects in mind we now discuss the results of our in-situ neutron diffraction study which we performed to investigate the evolution of residual stresses during the equi-biaxial tensile deformation stage. A key advantage of the in-situ neutron diffraction measurements (Repper et al., 2013; Sofinowski et al., 2019; Van Petegem et al., 2016) is that they allow to probe the entire volume, i.e., they provide integral information throughout the sheet thickness of the cruciform specimen as opposed to conventional XRD measurements which only yield information from a surface layer with a thickness of a few microns.

Lattice strains determined during equi-biaxial loading as a function of the macroscopic deformation[5] for different grain families of types {110}, {211} and {220} are shown in Fig. 9. These three grain families are representative and were also selected for analysis as they exhibit the highest count of diffracted neutrons. With the help of elastic constants of the material, lattice strain values can in principle be converted into (residual) elastic stresses. While we did not explicitly perform this stress calculation, Fig. 9 can be interpreted as a (residual) stress-macroscopic strain diagram. Prior to loading, the three grain families exhibit some small negative lattice strains, which corresponds to negative/compressive residual stresses. Such residual stresses frequently occur in cold-rolled steel sheets. During equi-biaxial tensile loading, the evolution of all three curves for the {110}, {211} and {220} grain families is similar to that of a typical stress-strain-curve, with an elastic slope, work hardening and finally (elastic) load removal. As expected, during the biaxial tensile deformation, increasing tensile elastic strains/stresses in all grain families can be observed, which reach their maximum at the maximum macroscopic tensile strain. During load removal, lattice strains/stresses are decreased, following a linear slope. Most interestingly, after complete unloading, distinct negative lattice strains were measured in the center part of the biaxial sample. The corresponding residual stresses must of course be counter-balanced by tensile stresses in the adjacent material, ensuring net-zero resulting forces in the load-free sample. Still, the diffraction results clearly demonstrate that, although equi-biaxisal tensile loads were applied, compressive residual stresses ultimately remain in the center part of the sample after load removal. This development of macro-scale residual stresses is in line with the build-up of microstructural elastic back stresses inferred from our TEM and EBSD results and agrees well with results from previous studies (Van Petegem et al., 2016). Compressive residual stresses clearly are predominant in the bulk material after biaxial tensile loading. This result also fully agrees with our mechanical observations of the Bauschinger effect.

Finally, to provide experimental documentation of the evolution of macro-scale residual stresses during equi-biaxial tensile loading and the subsequent equi-biaxial compressive testing, we briefly discuss the corresponding XRD results. Stress values for the RD (σ_{xx}) and for the TD (σ_{yy}), respectively, are summarized in Table 1. All measurements were repeated at least once to improve statistical significance; standard deviations given in Table 1 were calculated from the complete data representing nine tilting angles and six azimuth angles used in each XRD experiment. The IS (i.e., prior to mechanical loading) exhibits compressive residual stresses of about -40 MPa in RD and -31 MPa in TD, which agrees with the neutron diffraction data (Fig. 9) and which demonstrates that in the IS,

[5] Note that during the biaxial tensile testing for the neutron diffraction measurements, the TD axis was also “harder” than the RD axis. Therefore, cross hardening effects may have occurred in this measurement with a similar contribution as in our previous biaxial tensile experiments.

Table 1
Build-up of residual stresses with different maximum equi-biaxial tensile strains (0.5 and 2.0 %, respectively) in RD, σ_{xx}, and in TD, σ_{yy}. The stages of biaxial deformation (a–c) are similar to those defined in Fig. 5d.

stage of deformssation	maximum tensile strain			
	0.5 %		2.0 %	
	residual stress in MPa			
	σ_{XX}(RD)	σ_{YY}(TD)	σ_{XX}(RD)	σ_{YY}(TD)
IS	-39.8 ± 7.1	-30.9 ± 7.1	-39.8 ± 7.1	-30.9 ± 7.1
a	152.7 ± 22.3	133.8 ± 22.3	96.6 ± 16.0	107.5 ± 15.8
b	-7.3 ± 4.9	-14.9 ± 5.7	-81.2 ± 9.3	-64.9 ± 9.3
c	-65.1 ± 11.2	-67.3 ± 11.2	-46.2 ± 13.1	-54.0 ± 13.1

residual stresses in the sample surface (as probed by XRD) and the bulk (analyzed by neutron diffraction) are quite similar. Interestingly, equi-biaxial tensile deformation to strains of 0.5 % (and subsequent unloading) leads to high tensile residual stresses of about 153 MPa in RD and 134 MPa in TD, respectively. Due to the equi-biaxial tensile testing procedure ("harder" axis vs "softer" axis), we observed differences in the stress-strain curves between TD and RD (Fig. 3). These differences can cause cross hardening effects in the material and result in higher residual stresses during multiaxial loading (Franz et al., 2009) and increased local misorientation as well as dislocation densities. Most importantly, the obvious deviation from the bulk measurements of compressive stresses discussed above is likely related to the evolution of stress gradients in thickness-direction of the sample, where tensile stresses in the surface layer are needed to counter-balance the compressive stress state in the bulk. Clearly, the presence of through-thickness stress gradients prohibits a direct interpretation of surface XRD data to represent the stress state in the bulk of the samples; nevertheless, their evolution during subsequent compressive loading (points b and c, Table 1) can be analyzed phenomenologically to further document changes of macro-scale residual stresses that occur in the latter stages of our experiments. Immediately after load reversal (stage b), we measured relatively small compressive residual stresses in both directions (-7 MPa in RD and -15 MPa in TD). Subsequent plastic deformation to 3.5 % in equi-biaxial compression (stage c) leads to an increase of the compressive residual stresses in the sample surface to -65 MPa in RD and -67 MPa in TD. The equi-biaxial deformation again causes higher residual stresses than the uniaxial deformation (see (Härtel et al., 2019)). The absolute values for equi-biaxial tensile loading (stage a) compared with equi-biaxial compressive loading (stage c) are higher. This can be related to the higher total plastic deformation in equi-biaxial compression (3.5 % vs. 0.5 %), which microstructurally correlates with the formation of substructures (as clearly visible in Fig. 7c) and hence reduces strain energy (Lewandowska, 2003; Vincze et al., 2005), ultimately decreasing residual stresses on the micro-scale as well as on the macro-scale.

Equi-biaxial tensile deformation up to 2.0 % also leads to tensile residual surface stresses of 97 MPa in RD and 108 MPa in TD. Compared to the 0.5 % condition, the residual stresses are lower. The load path change and subsequent yielding under compression (stage b) lead to compressive residual stresses of -81 MPa in RD and -65 MPa in TD. The difference between stage a and b for this condition is much higher than for the condition with 0.5 % maximum equi-biaxial tensile strain. Similar observations for uniaxial load cases (Härtel et al., 2019) could be attributed to elastic back stresses (Abel and Muir, 1972; Hu et al., 2017; Kostryzhev, 2009; Kostryzhev et al., 2010; Lee et al., 2013; Plumtree and Abdel-Raouf, 2001; Richards et al., 2011; Sleeswyk and Kemerink, 1985; Stout and Rollett, 1990; Xue et al., 2016; Zhu et al., 2013): especially pile-ups of dislocations in the vicinity of grain boundaries are sources for elastic back stresses (Lee et al., 2013; Xue et al., 2016; Zhu et al., 2013), and incorporating these effects can considerably improve spring back prediction in crystal plasticity simulations (Kim et al., 2012). The important influence of back stresses is also highlighted by the fact that for 2 % maximum equi-biaxial tensile strain the difference in XRD results between stages a and b is more pronounced than the difference between IS and a, even though more plastic deformation (2 % vs. 0.2 %) was applied. Further straining under equi-biaxial compressive loads leads to compressive residual surface stresses of -46 MPa in RD and -54 MPa in TD. This decrease in residual stresses correlates with the renewed formation of substructures (Figs. 6 and 8). While we emphasize again that the XRD results are not fully representative of the bulk stress states, our observations clearly indicate a distinct evolution of macro-scale residual stresses during equi-biaxial tensile loading followed by equi-biaxial compression. Our results thus demonstrate that the Bauschinger effect results from a complex interaction of multiple effects, including the annihilation of dislocation and dislocation substructures, the build-up of intergranular and intragranular residual stresses as well as their interaction with macro-scale residual stresses.

4. Summary and conclusions

The present study for the first time addresses the effect of equi-biaxial loading on Bauschinger effects in an IF sheet metal DC06 steel. Using advanced experimental setups, in-plane loading was used to perform equi-biaxial tensile testing, followed by equi-biaxial compression. The observed Bauschinger effects were documented to differ in terms of the Bauschinger effect factor from uniaxial tension-compression experiments. The macroscopic equi-biaxial Bauschinger effects and the corresponding microstructural changes were further analyzed by TEM, HR-EBSD, and XRD measurements. Specifically, we studied microstructural features associated with different characteristic stages of biaxial loading. Furthermore, we performed in-situ neutron diffraction during equi-biaxial tensile deformation and subsequent unloading. The key results can be summarized as follows:

- Electron microscopy showed that intergranular stresses (related to differences in the distribution of dislocations between different grains) were dominant at relatively small maximum tensile strains (0.5 %). Substructure formation, however, became more important at a maximum equi-biaxial strain of 2 %, which resulted in pronounced dislocation density variations within single grains and intragranular residual stresses.
- At both strain levels, dislocation pile-ups near grain boundaries were observed. Grain boundary-pile up interactions after load reversal likely resulted in the generation of (elastic) back stresses on the micro-scale. Diffraction results also highlighted the contribution of macro-scale residual stresses.
- The development of elastic residual stresses was also documented in in-situ neutron diffraction measurements. Although biaxial tensile loads were applied, we observed compressive residual stresses after unloading.

The results demonstrate that several microstructural (evolution of dislocation densities; formation of substructures; strain gradients in individual grains) and mechanical effects (build-up of residual stresses) simultaneously contribute to macroscopic Bauschinger effects in the IF DC06 sheet material. Considering further the results from our previously reported uniaxial experiments (Härtel et al., 2019) in combination with the equi-biaxial tension-compression tests reported here, it is worth noting that both in mechanical as well as in microstructural behavior the characteristics of the observed Bauschinger effects clearly differ between uniaxial and equi-biaxial load cases. For both uniaxial and equi-biaxial loading, elastic back stresses caused by intergranular residual stresses for small maximum tensile strains und intragranular residual stresses for slightly higher maximum tensile strains affect the observed Bauschinger effects. Differences were also observed regarding the dislocation densities and dislocation annihilation after load reversal. While for the uniaxial tests annihilation was not a main factor (GND density even slightly increased), we observed distinct annihilation resulting in a decrease of the GND densites for equi-biaxial investigations. Another difference was observed in the formation of substructures which already occurred for 2 % equi-biaxial tensile loading – in contrast to the 2 % uniaxial tensile load. Finally, we acknowledge that our study is considerably limited with respect to the strain paths used: we solely focused on equi-biaxial loading in tension and as well as in subsequent compression. Obviously, with a view to practical applications like sheet metal forming processes, it would be very interesting to also explore different strain paths (and load reversals), for instance, biaxial loading with ratios of 2:1 or 3:1. However, the specimen designs used in the present study do not allow for such experiments as the biaxial tensile sample was optimized specifically for equi-biaxial loading and strain distributions quickly become inhomogeneous when other load ratios are applied. Moreover, an analysis of Bauschinger effects necessitates an accurate estimation of stress values from the measured force data. While our equivalent cross-section approach works well for equi-biaxial loading, it, too, breaks down once loading differs from the equi-biaxial case studied here; without the use of stress values, Bauschinger effects cannot be quantified. Thus, there clearly is a need for the development of more versatile experimental approaches that allow for accurate stress and strain measurements for a wider range of strain paths, stress ratios, and different combinations of load cases when switching from tension to compression, as well as, ideally, generally larger maximum strains.

Martin F.-X. Wagner reports financial support was provided by German Research Foundation. Enrico Bruder reports financial support was provided by German Research Foundation.

CRediT authorship contribution statement

Markus Härtel: Conceptualization, Investigation, Formal analysis, Validation, Writing – original draft, Project administration. **Christian Illgen:** Investigation, Formal analysis, Writing – original draft. **Tobias Panzner:** Investigation, Formal analysis, Validation. **Enrico Bruder:** Investigation, Formal analysis, Validation, Writing – original draft, Funding acquisition. **Stefan Schmaltz:** Investigation, Formal analysis, Validation. **Steven Van Petegem:** Validation, Writing – original draft. **Kai Willner:** Validation, Resources, Supervision. **Karsten Durst:** Validation, Resources. **Helena van Swygenhoven:** Validation, Resources. **Martin F.-X. Wagner:** Conceptualization, Validation, Writing – original draft, Project administration, Funding acquisition.

Declaration of Competing Interest

The authors declare the following financial interests/personal relationships which may be considered as potential competing interests.

Data availability

Data will be made available on request.

Acknowledgments

The authors gratefully acknowledge funding by the German Research Foundation (Deutsche Forschungsgemeinschaft, DFG) in project WA 2602/12-1, funding of the high resolution TESCAN MIRA3 SEM in project 255944295 as well as publication OpenAccess funding of Chemnitz University of Technology. We further thank Marc Pügner for help with the XRD measurements and Anne Schulze for TEM support.

Supplementary materials

Supplementary material associated with this article can be found, in the online version, at doi:10.1016/j.ijplas.2022.103478.

References

Abel, A., Muir, H., 1972. The Bauschinger effect and discontinuous yielding. Philos. Mag. 26, 489–504. https://doi.org/10.1080/14786437208227444.

Ackermann, S., Kulawinski, D., Henkel, S., Biermann, H., 2014. Biaxial in-phase and out-of-phase cyclic deformation and fatigue behavior of an austenitic TRIP steel. Int. J. Fatigue 67, 123–133. https://doi.org/10.1016/J.IJFATIGUE.2014.02.007.

Ackermann, S., Lippmann, T., Kulawinski, D., Henkel, S., Biermann, H., 2015. Biaxial fatigue behavior of a powder metallurgical TRIP steel 34, 580–589. 10.3221/IGF-ESIS.34.64.

Allain-Bonasso, N., Wagner, F., Berbenni, S., Field, D.P., 2012. A study of the heterogeneity of plastic deformation in IF steel by EBSD. Mater. Sci. Eng. A 548, 56–63. https://doi.org/10.1016/j.msea.2012.03.068.

Bagherpour, E., Reihanian, M., Ebrahimi, R., Qods, F., Miyamoto, H., 2020. Role of strain reversal in microstructure and texture of pure al during non-monotonic simple shear straining. Crystals 10, 1–15. https://doi.org/10.3390/cryst10100926 (Basel).

Banabic, D., Barlat, F., Cazacu, O., Kuwabara, T., 2020. Advances in anisotropy of plastic behaviour and formability of sheet metals. Int. J. Mater. Form. 13, 749–787. https://doi.org/10.1007/s12289-020-01580-x.

Barlat, F., Maeda, Y., Chung, K., Yanagawa, M., Brem, J.C., Hayashida, Y., Lege, D.J., Matsui, K., Murtha, S.J., Hattori, S., Becker, R.C., Makosey, S., 1997. Yield function development for aluminum alloy sheets. J. Mech. Phys. Solids 45, 1727–1763. https://doi.org/10.1016/S0022-5096(97)00034-3.

Bate, P.S., Wilson, D.V, 1986. Analysis of the bauschinger effect. Acta Metall. 34, 1097–1105. https://doi.org/10.1016/0001-6160(86)90220-8.

Bauschinger, J., 1886. Über die veränderung der elastizitätsgrenze und der festigkeit des eisens und stahls durch strecken und quetschen, durch erwärmen und abkühlen und durch oftmals wiederholte Beanspruchung. Mitt. Mech. Techn. Lab. K. Techn. Hochsch. München 13, 108–112.

Bhaskar, L.K., Kumar, G., Srinivasan, N., Kumar, R., 2021. Design and development of a miniaturized multiaxial test setup for in situ x-ray diffraction experiments. Rev. Sci. Instrum. 92, 015116 https://doi.org/10.1063/5.0031805.

Boger, R.K., Wagoner, R.H., Barlat, F., Lee, M.G., Chung, K., 2005. Continuous, large strain, tension/compression testing of sheet material. Int. J. Plast. 21, 2319–2343. https://doi.org/10.1016/j.ijplas.2004.12.002.

Brown, L.M., 1977. Orowan's explanation of the Bauschinger effect. Scr. Metall. 11, 127–131. https://doi.org/10.1016/0036-9748(77)90291-5.

Bruschi, S., Altan, T., Banabic, D., Bariani, P.F., Brosius, A., Cao, J., Ghiotti, A., Khraisheh, M., Merklein, M., Tekkaya, A.E., 2014. Testing and modelling of material behaviour and formability in sheet metal forming. CIRP Ann. Manuf. Technol. 63, 727–749. https://doi.org/10.1016/j.cirp.2014.05.005.

Buckley, S.N., Entwistle, K.M., 1956. The bauschinger effect in super-pure aluminum single crystals and polycrystals. Acta Metall. 4, 352–361. https://doi.org/10.1016/0001-6160(56)90023-2.

Caceres, C.H., Griffiths, J.R., Reiner, P., 1996. The influence of microstructure on the bauschinger effect in an Al-Si-Mg casting alloy. Acta Mater. 44, 15–23. https://doi.org/10.1016/1359-6454(95)00171-6.

Clausmeyer, T., Gerstein, G., Bargmann, S., Svendsen, B., van den Boogaard, A.H., Zillmann, B., 2013. Experimental characterization of microstructure development during loading path changes in bcc sheet steels. J. Mater. Sci. 48, 674–689. https://doi.org/10.1007/s10853-012-6780-9.

Copreaux, J., Lanteri, S., Schmitt, J.-H., 1993. Effect of precipitation on the development of dislocation substructure in low carbon steels during cold deformation. Mater. Sci. Eng. A 164, 201–205. https://doi.org/10.1016/0921-5093(93)90662-X.

Demir, E., Raabe, D., 2010. Mechanical and microstructural single-crystal Bauschinger effects: observation of reversible plasticity in copper during bending. Acta Mater. 58, 6055–6063. https://doi.org/10.1016/j.actamat.2010.07.023.

Deng, N., Kuwabara, T., Korkolis, Y.P., 2015. Cruciform specimen design and verification for constitutive identification of anisotropic sheets. Exp. Mech. 55, 1005–1022. https://doi.org/10.1007/s11340-015-9999-y.

Feaugas, X., 1999. On the origin of the tensile flow stress in the stainless steel AISI 316L at 300K: back stress and effective stress. Acta Mater. 13, 3617–3632. https://doi.org/10.1016/S1359-6454(99)00222-0.

Franz, G., Abed-Meraim, F., Ben Zineb, T., Lemoine, X., Berveiller, M., 2009. Role of intragranular microstructure development in the macroscopic behavior of multiphase steels in the context of changing strain paths. Mater. Sci. Eng. A 517, 300–311. https://doi.org/10.1016/j.msea.2009.03.074.

Gao, H., Huang, Y., 2003. Geometrically necessary dislocation and size dependent plasticity. Scr. Mater. 48, 113–118. https://doi.org/10.1016/S1359-6462(02)00329-9.

Güner, A., Zillmann, B., Lampke, T., Tekkaya, A.E., 2013. In-situ stress analysis with X-Ray diffraction for yield locus characterization of sheet metals. 10.1063/1.4850059.

Gupta, S.P., Kodali, S.P., 1976. The effect of pre-strain on the Bauschinger effect. Scr. Metall. 10, 111–114. https://doi.org/10.1016/0036-9748(76)90131-9.

Hanabusa, Y., Takizawa, H., Kuwabara, T., 2013. Numerical verification of a biaxial tensile test method using a cruciform specimen. J. Mater. Process. Technol. 213, 961–970. https://doi.org/10.1016/j.jmatprotec.2012.12.007.

Hannon, A., Tiernan, P., 2008. A review of planar biaxial tensile test systems for sheet metal. J. Mater. Process. Technol. 198, 1–13. https://doi.org/10.1016/j.jmatprotec.2007.10.015.

Härtel, M., Bohne, B., Wagner, M.F.-X., 2017. Microstructural evolution during tension-compression in-plane deformation of a pure aluminum sheet. In: In: Proceedings of the IOP Conference Series: Materials Science and Engineering 181. https://doi.org/10.1088/1757-899X/181/1/012024.

Härtel, M., Illgen, C., Bruder, E., Frint, P., Wagner, M.F.-X., 2019. Materials science & engineering a microstructural evolution during uniaxial tension-compression in-plane deformation of an IF steel. Mater. Sci. Eng. A 744, 652–660. https://doi.org/10.1016/j.msea.2018.12.073.

Härtel, M., Illgen, C., Frint, P., Wagner, M.F.-X., 2018. On the PLC effect in a particle reinforced AA2017 alloy. Metals. https://doi.org/10.3390/met8020088 (Basel) 8, 88.

Härtel, M., Illgen, C., Wagner, M.F.-X., 2016. Experimental evaluation of Bauschinger effects during tension-compression in-plane deformation of sheet materials. IOP Conf. Ser. Mater. Sci. Eng. 118 https://doi.org/10.1088/1757-899X/118/1/012018.

Härtel, M., Pfeiffer, S., Schmaltz, S., Söhngen, B., Kulawinski, D., Willner, K., Henkel, S., Biermann, H., Wagner, M.F.-X., 2018. On the identification of an effective cross section for a cruciform specimen. Strain. https://doi.org/10.1111/str.12257.

Hasegawa, T., Yakou, T., Karashima, S., 1975. Deformation behaviour and dislocation structures upon stress reversal in polycrystalline aluminium. Mater. Sci. Eng. 20, 267–276. https://doi.org/10.1016/0025-5416(75)90159-7.

Hou, Y., Lee, M.-G., Lin, J., Min, J., 2022. Experimental characterization and modeling of complex anisotropic hardening in quenching and partitioning (Q&P) steel subject to biaxial non-proportional loadings. Int. J. Plast. 156, 103347 https://doi.org/10.1016/j.ijplas.2022.103347.

Hu, X., Jin, S., Zhou, H., Yin, Z., Yang, J., Gong, Y., Zhu, Y., Sha, G., Zhu, X., 2017. Bauschinger effect and back stress in gradient Cu-Ge alloy. Metall. Mater. Trans. A 48, 3943–3950. https://doi.org/10.1007/s11661-017-4176-9.

Hughes, D.A., Hansen, N., Bammann, D.J., 2003. Geometrically necessary boundaries, incidental dislocation boundaries and geometrically necessary dislocations. Scr. Mater. 48, 147–153. https://doi.org/10.1016/S1359-6462(02)00358-5.

Jeong, Y., Gnäupel-Herold, T., Barlat, F.G., Iadicola, M., Creuziger, A., Lee, M.G., 2015. Evaluation of biaxial flow stress based on elasto-viscoplastic self-consistent analysis of X-ray diffraction measurements. Int. J. Plast. 66, 103–118. https://doi.org/10.1016/j.ijplas.2014.06.009.

Johnson, P.E., Schmitt, J.H., Vincent, S.A., Morris, J.W., 1990. The effect of prestrain temperatures on dislocation cell formation and subsequent tensile behavior in low carbon steel sheets. Scr. Metall. Mater. 24, 1447–1452. https://doi.org/10.1016/0956-716X(90)90412-A.
Kim, J.H., Kim, D., Barlat, F., Lee, M.-G., 2012. Crystal plasticity approach for predicting the Bauschinger effect in dual-phase steels. Mater. Sci. Eng. A 539, 259–270. https://doi.org/10.1016/j.msea.2012.01.092.
Knoerr, L., Sever, N., McKune, P., Faath, T., 2013. Cyclic tension compression testing of AHSS flat specimens with digital image correlation system 654, 654–658. 10.1063/1.4850057.
Kostryzhev, A.G., 2009. Bauschinger Effect in Nb and V Microalloyed Line Pipe Steels. University of Birmingham.
Kostryzhev, A.G., Strangwood, M., Davis, C.L., 2010. Bauschinger effect in microalloyed steels: part I. Dependence on dislocation-particle interaction. Metall. Mater. Trans. A 41, 1399–1408. https://doi.org/10.1007/s11661-010-0196-4.
Kulawinski, D., Ackermann, S., Glage, A., Henkel, S., Biermann, H., 2011a. Biaxial low cycle fatigue behavior and martensite formation of a metastable austenitic cast TRIP steel under proportional loading 82, 1141–1148. 10.1002/srin.201100111.
Kulawinski, D., Henkel, S., Holländer, D., Thiele, M., Gampe, U., Biermann, H., 2014. Fatigue behavior of the nickel-base superalloy Waspaloy™ under proportional biaxial-planar loading at high temperature. Int. J. Fatigue 67, 212–219. https://doi.org/10.1016/J.IJFATIGUE.2014.02.005.
Kulawinski, D., Hoffmann, M., Weidner, A., Lippmann, T., Lamprecht, G., Henkel, S., Biermann, H., 2017. Fatigue behaviour of 16Mo3 steel at elevated temperatures under uniaxial as well as biaxial-planar loading 909–923. 10.1111/ffe.12551.
Kulawinski, D., Nagel, K., Henkel, S., Hübner, P., Fischer, H., Kuna, M., Biermann, H., 2011b. Characterization of stress–strain behavior of a cast TRIP steel under different biaxial planar load ratios. Eng. Fract. Mech. 78, 1684–1695. https://doi.org/10.1016/j.engfracmech.2011.02.021.
Kuwabara, T., Nagata, K., Nakako, T., 2001. Measurement and analysis of the Bauschinger effect of sheet metals subjected to in-plane stress reversals. Proc. AMPT 1, 407–412. https://doi.org/10.1016/S0924-0136(98)00155-1.
Laukonis, J.V., Ghosh, A.K., 1978. Effects of strain path changes on the formability of sheet metals. Metall. Trans. A 9, 1849–1856. https://doi.org/10.1007/BF02663419.
Lee, M.G., Kim, J.H., Kim, D., Seo, O.S., Nguyen, N.T., Kim, H.Y., 2013. Anisotropic hardening of sheet metals at elevated temperature: tension-compressions test development and validation. Exp. Mech. https://doi.org/10.1007/s11340-012-9694-1.
Lee, S.W., Jennings, A.T., Greer, J.R., 2013. Emergence of enhanced strengths and Bauschinger effect in conformally passivated copper nanopillars as revealed by dislocation dynamics. Acta Mater. 61, 1872–1885. https://doi.org/10.1016/j.actamat.2012.12.008.
Lewandowska, M., 2003. Dependence of the deformation microstructure of aluminium alloys on the strain path. Mater. Chem. Phys. 81, 555–557. https://doi.org/10.1016/S0254-0584(03)00073-7.
Liao, J., Xue, X., Lee, M.G., Barlat, F., Vincze, G., Pereira, A.B., 2017. Constitutive modeling for path-dependent behavior and its influence on twist springback. Int. J. Plast. 93, 64–88. https://doi.org/10.1016/j.ijplas.2017.02.009.
Littlewood, P.D., Britton, T.B., Wilkinson, A.J., 2011. Geometrically necessary dislocation density distributions in Ti-6Al-4V deformed in tension. Acta Mater. 59, 6489–6500. https://doi.org/10.1016/j.actamat.2011.07.016.
Marcadet, S.J., Mohr, D., 2015. Effect of compression-tension loading reversal on the strain to fracture of dual phase steel sheets. Int. J. Plast. 72, 21–43. https://doi.org/10.1016/j.ijplas.2015.05.002.
Margolin, H., Hazaveh, F., Yaguchi, H., 1978. The grain boundary contribution to the bauschinger effect. Scr. Metall. 12, 1141–1145. https://doi.org/10.1016/0036-9748(78)90091-1.
Masing, G., 1926. Berechnung von dehnungs- und Stauchungslinien auf Grund von inneren Spannungen BT - Wissenschaftliche Veröffentlichungen aus dem Siemens-Konzern. 10.1007/978-3-662-24683-2_10.
Mehner, T., Bauer, A., Härtel, S., Awiszus, B., Lampke, T., 2018. Residual-stress evolution of cold-rolled DC04 steel sheets for different initial stress states. Finite Elements in. Anal. Des. 144, 76–83. https://doi.org/10.1016/j.finel.2017.11.006.
Mughrabi, H., 1983. Dislocation wall and cell structures and long-range internal stresses in deformed metal crystals. Acta Metall. 31, 1367–1379. https://doi.org/10.1016/0001-6160(83)90007-X.
Muhammad, W., Brahme, A.P., Kang, J., Mishra, R.K., Inal, K., 2017. Experimental and numerical investigation of texture evolution and the effects of intragranular backstresses in aluminum alloys subjected to large strain cyclic deformation. Int. J. Plast. 93, 137–163. https://doi.org/10.1016/j.ijplas.2016.11.003.
Mulder, J., Eyckens, P., van den Boogaard, A.H., 2015. Differential hardening in IF steel - Experimental results and a crystal plasticity based model. 8th Forming Technology Forum.
Nye, J.F., 1953. Some geometrical relations in dislocated crystals. Acta Metall. 1, 153–162. https://doi.org/10.1016/0001-6160(53)90054-6.
Ogihara, Y., Minote, T., Ishiwatari, A., Tamai, Y., 2020. -plane biaxial compression test on 780MPa cold rolled sheet steel. Procedia Manuf. Elsevier 1429–1433. https://doi.org/10.1016/j.promfg.2020.04.307. B.V.
Pantleon, W., 2008. Resolving the geometrically necessary dislocation content by conventional electron backscattering diffraction. Scr. Mater. 58, 994–997. https://doi.org/10.1016/j.scriptamat.2008.01.050.
Peeters, B., Kalidindi, S.R., Teodosiu, C., Houtte, P.V, Aernoudt, E., 2002. A theoretical investigation of the influence of dislocation sheets on evolution of yield surfaces in single-phase B.C.C. polycrystals. J. Mech. Phys. Solids 50, 783–807. https://doi.org/10.1016/S0022-5096(01)00094-1.
Piao, K., Lee, J.K., Kim, J.H., Kim, H.Y., Chung, K., Barlat, F., Wagoner, R.H., 2012. A sheet tension/compression test for elevated temperature. Int. J. Plast. 38, 27–46. https://doi.org/10.1016/j.ijplas.2012.03.009.
Plumtree, A., Abdel-Raouf, H.A., 2001. Cyclic stress–strain response and substructure. Int. J. Fatigue 23, 799–805. https://doi.org/10.1016/S0142-1123(01)00037-8.
Rauch, E.F., 1997. The stresses and work hardening rates of mild steel with different dislocation patterns. Mater. Sci. Eng. A 234, 653–656. https://doi.org/10.1016/S0921-5093(97)00357-2.
Rauch, E.F., Schmitt, J.-H., 1989. Dislocation substructures in mild steel deformed in simple shear. Mater. Sci. Eng. A 113, 441–448. https://doi.org/10.1016/0921-5093(89)90331-6.
Repper, J., Niffenegger, M., van Petegem, S., Wagner, W., van Swygenhoven, H., 2013. *In situ* biaxial mechanical testing at the neutron time-of-flight diffractometer POLDI. Mater. Sci. Forum 60–65. https://doi.org/10.4028/www.scientific.net/MSF.768-769.60, 768–769.
Rsichards, M.D., Van Tyne, C.J., Matlock, D.K., 2011. The influence of dynamic strain aging on resistance to strain reversal as assessed through the Bauschinger effect. Mater. Sci. Eng. A 528, 7926–7932. https://doi.org/10.1016/j.msea.2011.07.015.
Ruggles, T.J., Fullwood, D.T., 2013. Estimations of bulk geometrically necessary dislocation density using high resolution EBSD. Ultramicroscopy 133, 8–15. https://doi.org/10.1016/j.ultramic.2013.04.011.
Schmaltz, S., Willner, K., 2014. Comparison of different biaxial tests for the inverse identification of sheet steel material parameters. Strain 50, 389–403. https://doi.org/10.1111/str.12080.
Schmaltz, S., Willner, K., 2013. Material parameter identification utilizing optical full-field strain measurement and digital image correlation 13, 2–6. 10.11395/jjsem.13.s120.
Schmitt, J.H., Baudelet, B., 1985. Dislocation substructures and yield strength of prestrained low carbon steel sheets BT - strength of metals and alloys (ICSMA 7). 10.1016/B978-0-08-031642-0.50043-X.
Sleeswyk, A.W., Kemerink, G.J., 1985. Similarity of the Bauschinger effect in Cu, Al and Ni. Scr. Metall. 19, 471–476. https://doi.org/10.1016/0036-9748(85)90116-4.
Sofinowski, K., Panzner, T., Kubenova, M., Čapek, J., Van Petegem, S., Van Swygenhoven, H., 2019. *In situ* tension-tension strain path changes of cold-rolled Mg AZ31B. Acta Mater. 164, 135–152. https://doi.org/10.1016/j.actamat.2018.10.033.
Stout, M.G., Rollett, A.D., 1990. Large-strain Bauschinger effects in fcc metals and alloys. Metall. Trans. A 21, 3201. https://doi.org/10.1007/BF02647315.
Stuhr, U., 2005. Time-of-flight diffraction with multiple pulse overlap. Part I: the concept. Nucl. Instrum. Methods. Phys. Res. A 545, 319–329. https://doi.org/10.1016/j.nima.2005.01.320.

Stuhr, U., Spitzer, H., Egger, J., Hofer, A., Rasmussen, P., Graf, D., Bollhalder, A., Schild, M., Bauer, G., Wagner, W., 2005. Time-of-flight diffraction with multiple frame overlap Part II: the strain scanner POLDI at PSI. Nucl. Instrum. Methods. Phys. Res. A 545, 330–338. https://doi.org/10.1016/j.nima.2005.01.321.

Tan, Z., Magnusson, C., Persson, B., 1994. The Bauschinger effect in compression-tension of sheet metals. Mater. Sci. Eng. A 183, 31–38. https://doi.org/10.1016/0921-5093(94)90887-7.

Tsuru, T., Aoyagi, Y., Kaji, Y., Shimokawa, T., 2016. Heterogeneous plastic deformation and Bauschinger effect in ultrafine-grained metals: atomistic simulations. Modell. Simul. Mater. Sci. Eng. 24 https://doi.org/10.1088/0965-0393/24/3/035010.

Van Petegem, S., Wagner, J., Panzner, T., Upadhyay, M.V., Trang, T.T.T., Van Swygenhoven, H., 2016. *In-situ* neutron diffraction during biaxial deformation. Acta Mater. 105, 404–416. https://doi.org/10.1016/j.actamat.2015.12.015.

van Riel, M., van den Boogaard, A.H., 2007. Stress-strain responses for continuous orthogonal strain path changes with increasing sharpness. Scr. Mater. 57, 381–384. https://doi.org/10.1016/j.scriptamat.2007.05.005.

Vincze, G., Rauch, E.F., Gracio, J.J., Barlat, F., Lopes, A.B., 2005. A comparison of the mechanical behaviour of an AA1050 and a low carbon steel deformed upon strain reversal. Acta Mater. 53, 1005–1013. https://doi.org/10.1016/j.actamat.2004.10.046.

Wilkinson, A.J., Meaden, G., Dingley, D.J., 2006. High-resolution elastic strain measurement from electron backscatter diffraction patterns: New levels of sensitivity. Ultramicroscopy 106, 307–313. https://doi.org/10.1016/j.ultramic.2005.10.001.

Wright, S.I., Nowell, M.M., Field, D.P., 2011. A Review of strain analysis using electron backscatter diffraction. Microsc. Microanal. 17, 316–329. https://doi.org/10.1017/S1431927611000055.

Xiao, R., 2019. A review of cruciform biaxial tensile testing of sheet metals. Exp. Tech. 501–520. https://doi.org/10.1007/s40799-018-00297-6.

Xue, X., Liao, J., Vincze, G., Pereira, A.B., Barlat, F., 2016. Experimental assessment of nonlinear elastic behaviour of dual-phase steels and application to springback prediction. Int. J. Mech. Sci. 117, 1–15. https://doi.org/10.1016/j.ijmecsci.2016.08.003.

Yin, Q., Zillmann, B., Suttner, S., Gerstein, G., Biasutti, M., Tekkaya, A.E., Wagner, M.F.-X., Merklein, M., Schaper, M., Halle, T., Brosius, A., 2014. An experimental and numerical investigation of different shear test configurations for sheet metal characterization. Int. J. Solids Struct. 51, 1066–1074. https://doi.org/10.1016/j.ijsolstr.2013.12.006.

Zhang, R., Shao, Z., Shi, Z., Dean, T.A., Lin, J., 2021. Effect of cruciform specimen design on strain paths and fracture location in equi-biaxial tension. J. Mater. Process. Technol. 289, 116932 https://doi.org/10.1016/j.jmatprotec.2020.116932.

Zhu, D., Zhang, H., Li, D.Y., 2013. Influence of nanotwin boundary on the Bauschinger's effect in Cu: a molecular dynamics simulation study. Metall. Mater. Trans. A Phys. Metall. Mater. Sci. 44, 4207–4217. https://doi.org/10.1007/s11661-013-1752-5.

Zillmann, B., Härtel, M., Halle, T., Lampke, T., Wagner, M.F.-X., 2011. Flow behavior of automotive aluminum sheets during in-plane uniaxial and biaxial compression loading. In: Proceedings of the 10th International Conference on Technology of Plasticity.

Zillmann, B., Wagner, M.F.-X., Schmaltz, S., Schmidl, E., Lampke, T., Willner, K., 2014. Mechanical testing of thin metal sheets in biaxial compression.

Zillmann, B., Wagner, M.F.-X., Schmaltz, S., Schmidl, E., Lampke, T., Willner, K., Halle, T., 2015. In-plane biaxial compression and tension testing of thin sheet materials. Int. J. Solids Struct. https://doi.org/10.1016/j.ijsolstr.2015.03.031.